2022-12-01

Black And Brown Carbon Optical Characterization In The El Paso - Ciudad Juarez Airshed

Pamela I. Lara
University of Texas at El Paso

BLACK AND BROWN CARBON OPTICAL CHARACTERIZATION

IN THE EL PASO – CIUDAD JUAREZ AIRSHED

PAMELA I. LARA

Doctoral Program in Environmental Science and Engineering

APPROVED:

Rosa Fitzgerald, Ph.D., Chair

William Stockwell, Ph.D.

Marian Manciu, Ph.D.

Joshua Schwarz, Ph.D.

Stephen L. Crites, Jr., Ph.D.
Dean of the Graduate School

Dedication

To my parents, Rene and Gladys Lara, with all my love and gratitude.

BLACK AND BROWN CARBON OPTICAL CHARACTERIZATION IN THE EL PASO – CIUDAD JUAREZ AIRSHED

by

PAMELA I. LARA, MS.

DISSERTATION

Presented to the Faculty of the Graduate School of

The University of Texas at El Paso

in Partial Fulfillment

of the Requirements

for the Degree of

DOCTOR OF PHILOSOPHY

Doctoral Program in Environmental Science and Engineering

THE UNIVERSITY OF TEXAS AT EL PASO

December 2022

Acknowledgements

I would like to acknowledge my professor, Dr. Rosa Fitzgerald, for all her support, guidance, and contribution to this research, which is the culmination of all my several years of study. To my Dissertation Committee for their willingness to work with me. To my lab-mates (they kept me sane). To the NOAA Center for Atmospheric Science-Meteorology (NCAS-M), which is funded by the National Atmospheric Administration/Educational Partnership Program under cooperative Agreement #NA16SEC4810006. To TCEQ for their support with the instruments. To Dr. Joshua Schwarz and Dr. Joseph Katich, from NOAA Atmospheric Composition and Climate Processes, ACCP, Chemical Science Laboratory for those 12 weeks of training. And to my family.

Abstract

Black (EBC) and Brown (BrC) Carbon are ubiquitous constituents of atmospheric particulate matter that affect people's health, disrupt ecosystems, and modulate local and global climate. Tracking the local deposition and sources of these aerosol particles is essential to better understanding their multidimensional environmental impact. The main goal of the current study is to measure the absorption coefficient (B_{abs}) of particles within the Planetary Boundary Layer (PBL) of the El Paso (US)–Ciudad Juárez (Mexico) airshed and assess the contribution of black and brown carbon particles to the total optical absorption. Measurements were taken during winter (January, 2022), spring (May, 2022), and a summer-wildfire (August-September, 2021)- season to evaluate the optical properties of BC and non-$_{volatile}$ and low-$_{volatile}$ BrC. The summer-wildfire season presented the greatest variation in the Babs from the background values due to EBC and BrC rich smoke plumes arriving to this region from the US West seasonal wildfires. The winter season presented a variation from the background Babs in the late evening hours (3:00 PM to midnight) due to an increase of biofuel burning for heating driven by lower temperatures. The spring season presented variations according to the background Babs common to the region, as follows. It was found that the international bridges' vehicular traffic, characterized by hours of waiting time to cross back and forth between both cities, supplemented by other local anthropogenic activities, such as brick kiln emissions in Ciudad Juarez, have created a background of air pollution in this region. These pollutants include carbon monoxide, sulfur dioxide, nitrogen and nitric oxides, coarse and fine particulate matter dominated by BC and BrC. The absorption coefficients due to EBC and BrC of this background constitute what we have called a baseline EBC and BrC. Aided by two photoacoustic Extinctiometers (PAX), operating at 405 nm and 870 nm wavelengths, connected to a 340°C thermal denuder to remove non-refractory organics, the particles absorption characteristics were documented and evaluated to identify the impact of long-range transported emissions, from western wildfires, to the local occurrences during summer, as well as the winter and spring EBC and BrC Babs behavior. The Single Scattering Albedo and the

Absorption Ångstrom exponent were calculated for the three seasons. Of notice was a decrease in the Ångstrom Absorption exponent during the wildfire event days (eighteen events recorded) due to the aging process. The High-Resolution Rapid Refresh Smoke model, HRRR, and the Hybrid Single-Particle Lagrangian Integrated Trajectory model, HYSPLIT, were used to estimate the sources of the particles during the summer-wildfire season. Keywords: brown carbon; black carbon; troposphere; wildfires; photoacoustic measurements; HYSPLIT, planetary boundary layer

Table of Contents

Dedication iii

Acknowledgements v

Abstract vi

Table of Contents viii

List of Tables x

List of Figures xi

List of Illustrations xiv

Chapter 1: Introduction 1

1.1 Site Description and Terrain 4

1.2 Absorption Coefficient Baseline, Event Days, and Carbon Monoxide 5

1.3 Air Mass Trajectory Analysis 7

Chapter 2: Methodology and Instrumentation 7

2.1 Instrumentation 7

2.1.1 Photoacoustic Extinctiometer 7

2.1.2 Ceilometer 9

2.2 Instrument Calibration and Data Processing 10

2.2.1 Calibration procedure for PAX Scattering and Absorption 10

2.2.2 Brown Carbon Babs Derivation 11

2.2.3 Single Scattering Albedo and Ångstrom Exponent Calculation 12

Chapter 3: Analysis 14

3.1 EBC and BrC Winter Season Characterization 14

3.1.1 Single Scattering Albedo and the Ångstrom Exponent for the Winter Season 18

3.2 EBC and BrC Spring Season Characterization 20

3.2.1 The Single Scattering Albedo (SSA) and the Absorption Ångstrom Exponent for the Spring Season 23

3.3 EBC and BrC Summer Wildfire Seasonal Characterization 25

3.3.1 The Single Scattering Albedo (SSA) and the Absorption Ångstrom Exponent for the Summer Wildfire Season 31

3.3.2 HRRR and HYSPLIT for the Wildfire Event Days....33
3.3.3 Composite Synoptic Conditions and PBL Structure during the Wildfire Exceedance Events....36
3.4 Summary Graphs....38
Chapter 4: Discussion and Conclusions....42
References....46
Vita….....49

List of Tables

Table 1: The average and maximum values of the BC and BrC Babs (Babs, Mm^{-1}) for \the three prominent peaks in Figures 2a, 2b, and 3. 18
Table 2: The August and September event days where the smoke plumes output by a wildfire made their way to our region. The California wildfires were mainly in the north part of the state. The HRRR reported the plumes as $PM_{2.5}$ in micrograms per cubic meter through a color-coded volume. Most of the fires lasted for a couple of days. 26

List of Figures

Figure 1: The absorption coefficient, Babs, for January 2021, corresponding to the winter season characterization. 1a compares the Babs due to EBC from PAX 870 nm (left) and PAX 405 nm (right, blue). After 3:00 PM a clear increase in the Babs (~300% increment) is observed in both instruments. We concluded that this increment from its baseline (before 3:00 PM) was related to a decrease in ambient temperature. 1b shows the extrapolated BrC Babs that manifested the same behavior. The standard error was calculated for each data point (10 minutes of observation) and a binomial smoothing filter was applied. 16
Figure 2: PAX 870 nm, PAX 405 nm, and BrC Babs boxplots that show the spread of the data points. 2a presents the spread for the significant peak after 3:00PM for the EBC Babs of both instruments and for the extrapolated BrC Babs. 2b shows the general spread of the whole month of January for the three optical parameters indicated. 17
Figure 3: Carbon monoxide molar mixing ratios in parts per million by volume diurnally averaged over January 2022 data from the Texas Commission on Environmental Quality monitoring station at Chamizal National Park, CAM41. The graph has been temperature coded, with the lowest temperatures toward the blue-purple ends and higher temperatures toward the orange red. After 4:00 PM the temperatures start to decrease, and the CO concentration increases. 17
Figure 4: Daily averages of the single scattering albedo were calculated for January 2022 from the absorption and scattering coefficients due to EBC detected by the PAX 870 nm. The graph has a smoothing filter applied (binomial smoothing by Wave Metrics Igor Pro 8 platform). Each point represents a daily average, and the errors are the standard error associated with each point.
Figure 5: The absorption Ångstrom Exponent -Equation (1)- was calculated using the Babs at 405 nm and 870 nm with the data obtained by the PAX instruments. The values represent daily averages for the month of January, 2022. A binomial smoothing was applied (IGOR Pro 8) to show the shape of the data. 19
Figure 6: EBC Babs for 28 days of May, 2022. On the vertical axis, the absorption coefficient (units of inverse length), for the PAX 870 nm on the left, and 405 nm on the right (blue). The x-axis shows the diurnal averages for the 28 days of data (from midnight to midnight). Each point represents 10 minutes of observation plus the standard error for each 10-min point, and the graph has a binomial smoothing filter applied. 20
Figure 7: the absorption coefficient due to brown carbon, diurnal averages, for 28 days of May, 2022. The peaks and valleys are a representation of the BrC Babs emitted by the vehicles, commercial and particular, waiting to cross the border between 21
El Paso and Ciudad Juarez, and also by the BrC emitted by the brick kiln 21
common of Ciudad Juarez. Each point represents 10 minutes of observation 21
plus, the standard error for each 10-min point. The graph has a binomial smoothing filter applied.
Figure 8: A boxplot presenting the spreading of the data, from a median value. The BC Babs 405 (blue) presented the highest spreading of the data values. 22
Figure 9: The Carbon Monoxide diurnal averages (24-hour period) as detected by the Texas Commission on Environmental Quality, Chamizal National Park, Cam41. The units are parts per million by volume, ppmV, with values between 0.10 and 0.30, the values are temperature-coded, with red indicating the highest temperature (here around 90ºF), and purple, the lowest (around 70ºF). 23

Figure 10: The single scattering albedo for 28 days of May, 2022, as measured by the PAX 870 nm. The x-axis shows daily averages of the parameter displayed on the y-axis. Between the 5th and 15th of the month, the values showed a prominent decline, maybe related to the mixing and coating of the BC particles. The graph had a binomial smoothing filter applied. 24
Figure 11: The absorption Ångstrom exponent for 28 days of May, 2022, as measured by the PAX 870 nm. The first 15 days of the month were characterized by an increase in particles' size, which started to decrease on the second half. The graph had a binomial smoothing filter applied.
Figure 12: The baseline diurnal averages of the Babs for August and September of 2021. In black (left y-axis), the baseline as measured by PAX 870 nm with its highest peak of 1.003 1/Mm at around midnight and its lowest point of 0.6639 1/Mm at around 3:30 PM (local times). In blue (right y-axis), the baseline as measured by PAX 405 nm with its highest peak of 7.658 1/Mm at around 7:30 AM and lowest values of 3.860 1/Mm at around 3:30 PM. The graph has a smoothing filter applied (binomial smoothing by Wave Metrics Igor Pro 8 platform). The errors bars represent the standard error associated with each point. 26
Figure 13: Equivalent Black Carbon mass concentration measured in micrograms per cubic meter. The bold marking represents those eighteen event days when the wildfire plumes reached our instruments..... 27
Figure 14: (a) shows the diurnal averages of the Babs due to BC particles of the eighteen wildfire event days of the season. The values on the left y-axis (in black) of the graph were reported by the PAX 870 nm, and on the right y-axis (blue) were calculated from the 405 nm PAX. The graph has a binomial smoothing filter applied. The error bars in (a) represent the standard error associated with each averaged point. Boxplots were added to present the spread of the data over 10 minutes averages for three California wildfire event days, September 03, September 14, and September 16. (b) shows the data spread for the BC Babs PAX 870 nm while (c) shows the spread of the BC Babs calculated from the PAX 405 nm..... 29
Figure 15: (a) The inferred BrC Babs is graphed here for the diurnal averages of 1 August through 23 September 2021. The Babs displayed in red are due to BrC corresponding to the eighteen event days (BrC Babs WFE), and displayed in black is the baseline (BL), BrC Babs driven by pollution from vehicular traffic. The peaks agree with the costumery rush hour times... The graph has a smoothing filter applied. The error bars represent the standard error associated with each averaged point. (b) represents the spread of this data for three California wildfires event days..... 31
Figure 16: The Single Scattering Albedo (SSA) for September of 2021 was calculated using the PAX 870 instrument. The bold marking indicates the SSA of event days. Each point represents the average measurement for the day..... 31
Figure 17: The Absorption Ångstrom Exponent was calculated using the Babs as calculated by the PAX instruments at 405 nm and 870 nm. The black markings correspond to the daily averages of the days where no wildfire smoke arrived at the region and therefore represent the AAE for the basline. The red markings indicate the daily averages for the days when wildfire smoke was detected in the region - event days- (eighteen event days between August and September of 2021). The baseline AAE was not subtracted from the event days AAE, hence, the red markings indicate the AAE for the event days plus the background AAE..... 32
Figure 18: The HRRR and HYSPLIT analyses for 8 September 2021. (a) The HRRR map indicates the surface mass concentration, from purple at the origin of the wildfire (northern California and south Oregon) to light blue at its lowest concentrations. El Paso, located at the

western corner of the state of Texas received 2-8 micrograms per cubic meter of $PM_{2.5}$. (b) The HYSPLIT backward trajectories run for 72 hours at height 1, 1.5 and 2 km from the surface.... 35
Figure 19**:** The HRRR and HYSPLIT analyses for 9 September 2021. (a) The HRRR map indicates the surface mass concentration, from purple at the origin of the wildfire (northern California and south Oregon) to light blue at its lowest concentrations. El Paso, located at the western corner of the state of Texas received 2-8 micrograms per cubic meter of $PM_{2.5}$. (b) The HYSPLIT backward trajectories run for 72 hours at height 1, 1.5 and 2 km from the surface.... 36
Figure 20: The satellite composite of 7 September 2021, at 1500Z showing the presence of a high-pressure system over the study area (left), and 10 September 2021, at 03Z showing hurricane Olaf near the southern coast of Baja California. 37
Figure 21: PBL structure as observed on 06 and 07 September 2021. The shallow PBL on September seventeenth resulted from the sinking motion of the atmosphere due to the presence of a high-pressure region over the study area. 38
Figure 22: the Babs of the EBC particles as measured by the PAX 870 nm. The graph's legend indicates which plot trend belongs to each season characterization. The graph has a binomial smoothing filter applied. 39
Figure 23: the Babs of the EBC particles as derived from the PAX 405 nm. Each trend line is 2.148 times bigger that those of the PAX 870. The graph's legend indicates which plot trend belongs to each season. The graph has a binomial smoothing filter applied 39
Figure 24: BrC Babs as calculated from equation (3). Though the plotting has a binomial smoothing filter, the trends seem noisy, maybe because the mineral dust particles contributed more to the total Babs than we expected. The peaks agree with the rush hour times customary for this region..... 40
Figure 25: The SSA summary for the three seasons. Binomial smoothing filter applied 41
Figure 26: The AAE summary for the three seasons. Binomial smoothing filter applied..... 41

List of Illustrations

Illustration 1: El Paso and Ciudad Juarez terrain map with international border demarcation. The four main international bridges are indicated with a red . The instruments are located where the red heart-shape shows. (Google Maps El Paso, TX) 5
Illustration 2: A schematic of an extinctiometer, combining a nephelometer and a photoacoustic spectrometer. The green arrows show the airflow. The instruments' manual indicates a nominal flow rate of 1.0 L/min ±10% at 21 °C and 1 atm. 8
Illustration 3: (a) PAX 405 nm and PAX 870 nm lab set up. Between the instruments, the thermal denuder. The sample line tubing brings the airflow through the thermal denuder first. After the particles are denuded at 340ºC, the sampled airflow is passed to the PAX for analysis. (b) The outside tubes containing the sample lines have a cover and mesh protector as suggested by the manufacturer. 9
Illustration 4: The new Vaisala ceilometer CL51 located on the roof of the Physical Science building at UTEP 9

Chapter 1: Introduction

With its complex topography, the El Paso–Ciudad Juárez region is located between the United States and Mexico with a population of 2.7 million people [1–3]. This region is isolated, 500 km away distance from any other major city and it is representative of a desert urban area with complex terrain. This urban area's air quality is primarily impacted by carbonaceous particulate matter composed of black carbon (BC) and organic carbon (OC). When we discuss black carbon in the context of light absorbing material, we refer to it as BC in accordance with Petzold et al., Grange et al., and Andreae and Gelencser, who are consistent with terminology that is generally accepted by the aerosol community [4,5,8]. When we refer to our measurements of BC, we label them as equivalent black carbon, (EBC), to clarify that what we are measuring is optical absorption, and we are presenting this as the concentration of black carbon (with assumed optical properties) that would generate the same absorption [4,5]. Soot, a mixture of BC, OC, and sometimes mineral dust, is the primary component of particulate matter (PM) in this region [1,6,7]; however, PM in this region can also include coarse mass particles (probably mostly consisting of soil and windblown dust), elemental carbon, organic material, PM formed by atmospheric chemical reactions of anthropogenically and biological emitted organic compounds - anthropogenic secondary organic aerosol (anthropogenic SOA) , and biogenic secondary organic aerosol (biogenic SOA), ammonium nitrate, and ammonium sulfate [8]. Carbonaceous aerosol particle emissions are produced primarily from incomplete combustion, e.g., burning biomass and fossil fuels; however, other sources like cooking and industrial processes are also present.

The relative abundance of carbonaceous material in emissions is determined by flame presence and temperature [8,9]. Black carbon includes elemental carbon (EC), defined as the refractory component of carbonaceous particulate matter that does not volatilize in the air at

temperatures below 600^0 C, EC is produced by high-temperature flames and OC, which includes BrC, volatilizes in the air at temperatures below 400^0 C. Brown carbon is referred to as "brown" due to its optical properties, i.e., its color when emitted from burning material. It may include several organic compound classes such as alcohols, aromatics, di and tri organic acids, hydroxy acids, ketoacids, or sugars. Carbonaceous particles produced from gas-phase chemical reactions are known as secondary organic aerosols (SOA). The SOAs substantially affect human health, including injury to lung cells [10,11].

Carbonaceous particles are strong solar and terrestrial radiation absorbers, influencing visibility [12] and climate [13]and can lead to localized heating with subsequent increases in ambient temperatures. The absorption of UV radiation by carbonaceous aerosols may decrease the photolysis frequencies of ozone producing trace gases thus mitigating some of the increases in air pollution associated with global warming. Conversely, reductions in BC emissions designed to mitigate climate change may lead to increases in ozone and secondary particulate concentrations. Carbonaceous particles are heterogeneous sinks for ozone [14] and catalysts for the conversion of nitrogen dioxide (NO_2) to nitrous acid (HONO) [15], which may increase ozone formation during the early morning hours.

Past wildfire pollution studies in this region mainly focused on the effect of soot on human health [14] Chalbot et al. (2013) investigated the annual trends and spatiotemporal patterns of monthly 8-hour maximum ozone concentrations in the El Paso region and their associations with fires from 2001 to 2010 [17] [15]. However, no previous research has focused on detecting and quantifying the changes in the optical properties of particles due to BC and BrC in the El Paso–Juárez airshed, particularly during the Southwest's wildfire season. Furthermore, understanding

how the depth of the planetary boundary layer (PBL) impacts the carbonaceous particle mass concentrations is vital for better air quality forecasts [7].

The composition and size distribution of carbonaceous particles are expected to change in an aging smoke plume due to chemical reactions and physical processes occurring on their surface. Particle size distributions evolve with age as a result of the combined processes of particle coagulation, evaporation and sedimentation, yet the relative magnitude of these processes are uncertain and may be highly variable and very dependent on particle concentrations as well as meteorology [18]. The data presented in this paper do not include measurements of chemical composition and therefore we have relied on HYSPLIT simulations to provide some analysis of the origin and age of the measured particulate matter. We have, however, found evidence that the BC Absorption Angstrom Exponent becomes smaller in the summer season during a wildfire event, in particular for particles with mean diameters larger than 0.12 micrometers, which is one indication that the BC particles that arrive in the El Paso region are aged [18].

The main instruments used to produce this work were two Photoacoustic Extinctiometers-PAX- one at 405 nm and the other at 870 nm. -The primary objective of this study is to document the average optical properties of carbonaceous aerosols in the El Paso–Ciudad Juárez region and identify those periods when long-range transported aerosols from western wildfire exceed background levels. The results from this study will help improve local forecasts of air quality with a subsequent benefit to the health of the population. A secondary objective is the general characterization of the absorption coefficient, single scattering albedo, and Absorption Ångstrom Exponent common to this region. As such, we divided this study into three seasons: Winter, Spring, and Summer. A background characterization was obtained. We defined this background as the values not affected by specific circumstances, such as the wildfires in Summer or the temperature-related increments of Winter. The data we analyzed was denuded (at 340ºC) before entering the instruments. It is important for us to clarify that this work refers to denuded aerosols instead of

ambient aerosols. This work was partially based on the article *Winter and Wildfire Season Optical Characterization of Black and Brown Carbon in the El Paso-Ciudad Juárez Airshed,* published on July 29, 2022 by this author and collaborators. *Atmosphere* 2022, *13*(8), 1201; https://doi.org/10.3390/atmos13081201

1.1 Site Description and Terrain

El Paso (31º47'20" N, 106º25'20" W, 1145 m ASL), is located at the westernmost tip of the state of Texas, near a strategic mountain pass (Illustration 1). To its south is the Ciudad Juarez, Chihuahua, Mexico. Together they form one of the largest cross-border urban areas between the United States and Mexico [2]. The Rio Grande River, which originates from the Colorado mountains, separates the two cities that are linked by four bridges. The cities are located in the Chihuahua desert sharing a common airshed called the El Paso-Juarez airshed that has an average of 300 sunny days per year. Summers in this region are hot and dry, with mild and dry winters. The terrain is complex with mountain ranges to the northeast (Franklin mountains) and southwest (Juarez mountains) of the central El Paso-Juarez downtown area [2]. A sizable portion of the population resides in the downtown and surrounding areas, which are located in a central valley. The downtown central valley, located at the foothills of the mountains, is lower in elevation and has more uneven surfaces than its surroundings. The majority of concrete urban infrastructures, as well as the University of Texas at El Paso (UTEP) campus, are located in this area of the city. El Paso has deeper planetary boundary layers (from 3.5 to 4 km) in the summer and shallower (around 1-1.5 km) in the winter, a major factor affecting regional pollution events [2,3].

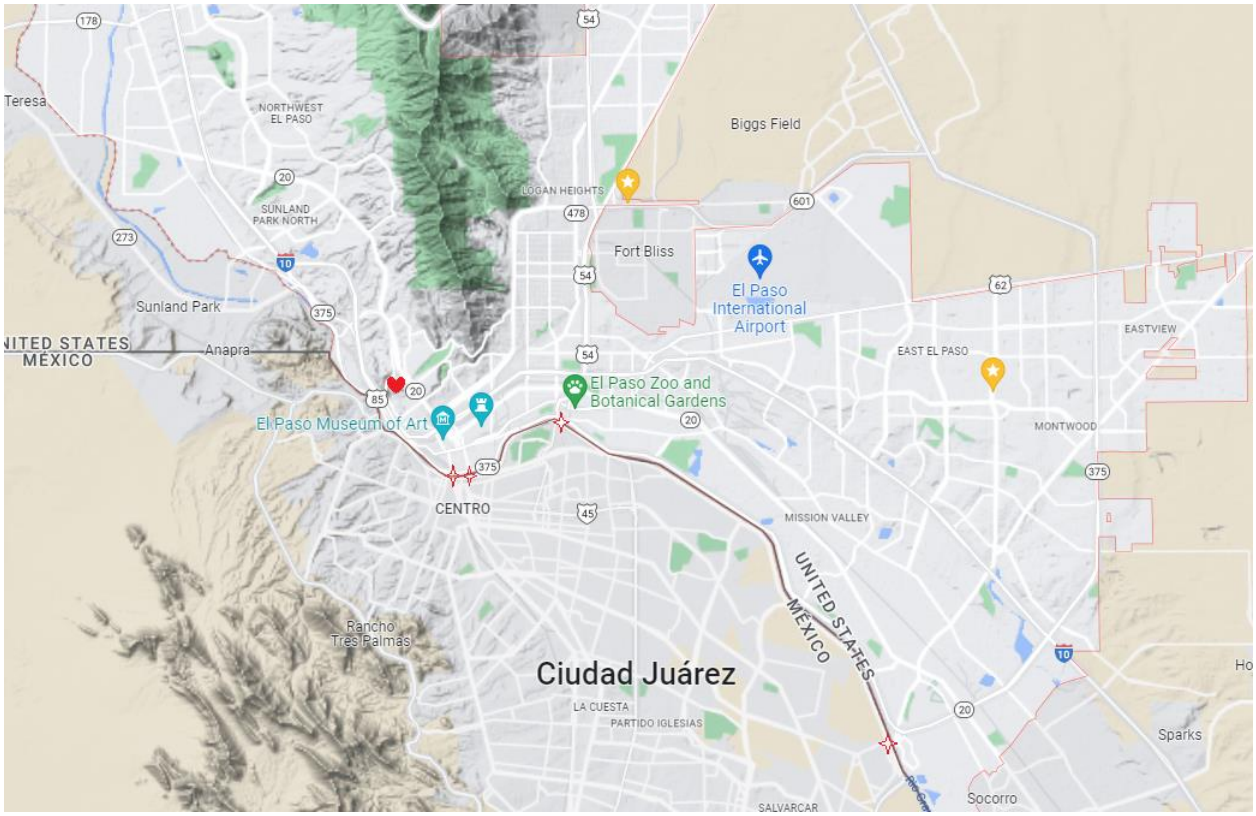

Illustration 1: El Paso and Ciudad Juarez terrain map with international border demarcation. The four main international bridges are indicated with a red . The instruments are located where the red heart-shape shows. (Google Maps El Paso, TX)

1.2 Absorption Coefficient Baseline, Event Days, and Carbon Monoxide

We have divided our study into three seasons represented by 4 to 6 weeks from each: the summer-wildfire season, from August 1 through September 23 2021; the winter season, with data collected 1-30, January 2022; and spring season, May 01 to May 05, and May 08 to May 30, 2022.

The three seasons include a background (defined in the Introduction as the values not affected by eventful circumstances, such as the wildfires in summer or the temperature-related increases of winter) average of the absorption coefficient, Babs, which we refer to as our season independent baseline: The idling traffic and long wait times at the US and Mexican border checkpoints (four bridges that connect the two cities) are a source of anthropogenic emissions due

to vehicular congestion. Besides the personal-use vehicles, there is a high density of commercial semi-trucks transporting goods to and from each country. The pollution produced by this situation has been studied in detail [24–26]. In addition to vehicular traffic, there are several brick kilns in Ciudad Juarez. In the 2012 *Environmental Assessment of Brick Kilns in Chihuahua State, México, Using Digital Cartography,* by Corral and De La Mora, [27], it is mentioned that a traditional brick kiln outputs ca. 86 kg of particulate matter during a 12-hour production period, and that the fuel used to produce the bricks "…varies according to what is available for brick makers and includes wood, recycled motor oil, coal, fuel oil, diesel, tires, trash and plastics among others."

For the Summer Wildfire Season, we have designated "event days" as those days when smoke plumes produced by wildfires in the US West Coast arrived and persisted at our region. These events were identified with the help of HRRR and HYSPLIT platforms. Table 2 contain eighteen event days, with the wildfire source listed as well. California wildfires were the main source with sixteen days.

The Texas Commission on Environmental Quality, TCEQ, has several air quality (AQ) monitoring stations across El Paso, including the CAM41, located at the Chamizal National Memorial Park. The CAM41 monitoring station provides valuable information, including the hourly average concentration of carbon monoxide, CO, reporting its molar mixing ratios in parts per million per volume. These data helped us in the analysis of our measurements since CO levels and BC/BrC levels have similar sources and are well correlated [28]. We added the TCEQ CO graph for the summer, winter, and spring season, with temperature embed coding as reference, especially for winter as, we claim, there is a decrease in temperature→increase in CO→ increase in BC and BrC relation.

1.3 Air Mass Trajectory Analysis

The High-Resolution Rapid Refresh (HRRR) is an atmospheric model developed by the National Oceanic and Atmospheric Administration (NOAA), with a real-time spatial and temporal resolution of 3 km and 1 hr. The model is initialized with 3 km grids and 3 km radar data assimilation. This study extensively used HRRR-smoke graphics (rapidrefresh.noaa.gov/hrrr/HRRRsmoke/) to obtain the near-surface smoke plumes trajectories. The 72-hour backward air parcel trajectories were calculated using the Hybrid Single-Particle Lagrangian Integrated Trajectory Model (HYSPLIT) version 4 to trace the trajectories of air masses carrying smoke from the wildfires on the US west coast to El Paso [31]. We employed HYSPLIT to estimate the source of these air masses as a complementary model to the HRRR.

Chapter 2: Methodology and Instrumentation

2.1 Instrumentation

2.1.1 Photoacoustic Extinctiometer

For our data collection, we used two Photoacoustic Extinctiometers, 405 nm and 870 nm (PAX, Droplet Measurement Technologies, DMT, Longmont, CO.). The PAX 405 nm was used to measure the black and brown carbon Babs. The PAX 870 nm was used for the black carbon absorption coefficient detection. These PAX combine both a nephelometer and a photoacoustic spectrometer, as seen in Illustration 2.

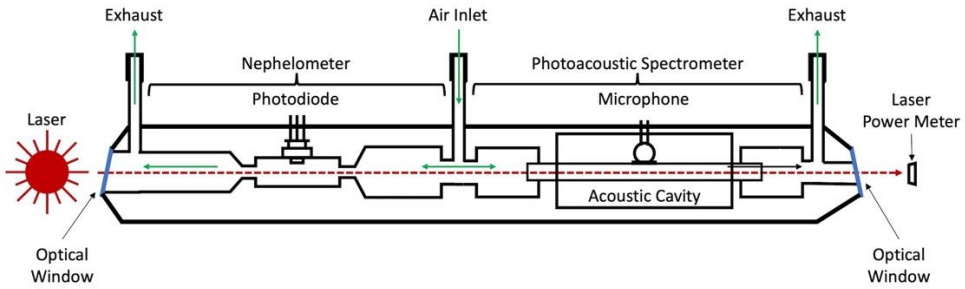

Illustration 2: A schematic of an extinctiometer, combining a nephelometer and a photoacoustic spectrometer. The green arrows show the airflow. The instruments' manual indicates a nominal flow rate of 1.0 L/min ±10% at 21 °C and 1 atm.

An oscillating-intensity laser beam passes through chambers of the nephelometer and photoacoustic spectrometer then exits to illuminate the laser power monitor. As the air enters the instrument it is divided into two airflows, one that enters the nephelometer chamber while the other flows through the photoacoustic chamber. In the nephelometer chamber some fraction of the scattered light is collected and focused onto a photodiode that converts the photons to and electrical signal that is digitized and recorded. In the photoacoustic chamber, particles that absorb light at the 405 or 870 nm wavelengths will increase in temperature as the absorbed energy is transformed to heat. Because the laser intensity is oscillating, the particles heat and cool, amplifying a standing acoustic pressure wave that is detected by the microphone in this chamber. The intensity of this pressure wave is converted to Babs through calibration. We connected both PAX instruments to a thermal denuder, a 40 cm stainless steel tube [20] that we kept at 340°C to remove non-refractory compounds..

. Both instruments are located inside of Atmospheric Physics lab, room 323 of the Physical Science building at the University of Texas at El Paso. A set of samples lines systems (~ 2 meters of tubing material approved by the manufacturer) connect the instruments to the exterior through the roof of the lab to collect/bring the airflow to the PAX's chambers. Illustrations 3a and 3b show the interior and exterior set up for both PAX.

(a) (b)

Illustration 3: (a) PAX 405 nm and PAX 870 nm lab set up. Between the instruments, the thermal denuder. The sample line tubing brings the airflow through the thermal denuder first. After the particles are denuded at 340ºC, the sampled airflow is passed to the PAX for analysis. (b) The outside tubes containing the sample lines have a cover and mesh protector as suggested by the manufacturer.

2.1.2 Ceilometer

We employed a Vaisala ceilometer, model CL51 (Illustration 4), located on the campus of the University of Texas at El Paso (UTEP) to measure the vertical distribution of backscattered light by atmospheric particles and to find the top of the PBL. The ceilometer has been in constant operation since 2020 [2,22]. The CL51 has a vertical range of 15 km and temporal and spatial resolutions of 16 s and 10 m, respectively. The laser used by the ceilometer is a semi-conductor InGaAs diode laser with a 905 ± 5 nm wavelength and three μJ pulse energy frequency of 6.5 kHz. The measured signals were processed using Vaisala's proprietary boundary layer software to calculate the PBL height (PBLH) using gradient methodology. Hourly averaged values of the PBLH were used for the analysis in this work.

Illustration 4: The new Vaisala ceilometer CL51 located on the roof of the Physical Science building at UTEP

2.2 Instrument Calibration and Data Processing

2.2.1 Calibration procedure for PAX Scattering and Absorption

The calibration of the PAX is a two-step process by which the scattering coefficient is first derived followed by that of the Babs. As shown in the diagram of the PAX in Figure 1, the PAX projects a laser beam through the sample cavity where the sample air is flowing. This beam falls on a photodetector that is measuring the photon density, which is also a measure of the light extinction by the particles. By definition, the extinction coefficient is proportional to the Napierian logarithm of the decrease in light intensity, i.e. $B_{ext} \sim -\ln[I/I0]$, where I0 in this case is the signal from the photodetector when no particles are present and I is the value when there are particles. The B_{scat} is calculated by first determining the raw scattering (background) of the instrument - Calibrated readings from the photomultiplier tube divided by the laser power- then air sampled scattering is calculated and subtracted from the raw scattering. The extinction coefficient is the sum of the scattering and absorption coefficients so when particles that only scatter light are introduced into the PAX chamber, extinction is equal to scattering only. The calibration procedure introduces a poly-dispersed spray of ammonium sulfate, over a range of concentrations, into the PAX while recording the voltage from the photodetector. A linear regression between -ln[I/I0] vs the signal measured by the scattering detector produces the calibration coefficient for deriving the scattering coefficient, since ammonium sulfate is non-absorbing at all wavelengths as discussed by Washenfelder et al, 2013 and references therein [23].

To calculate the Babs, highly light absorbing particles are produced from the combustion of a commercial gas called MAP/Pro, which is primarily composed of propylene and propane. As with the ammonium sulfate, these particles are introduced over a range of concentrations and the outputs of the absorption, scattering and laser monitors are recorded. Since the BC particles also

scatter light, the absorption is calculated as the difference between extinction measured by the laser monitor and light scattering from the PAX scattering detector. The calibration coefficient is subsequently derived through linear regression.

2.2.2 Brown Carbon Babs Derivation

While BC absorbs at all wavelengths, BrC primarily absorbs in the ultraviolet (UV). For the purposes of deriving BrC from the PAX measurements, we assume that BC is the primary absorber at 870 nm and that BC and BrC absorb at 405 nm and follow a well-known methodology to extract the absorption due to BrC only. Previous studies, e.g., Kirchstetter et al. [29] (and references there in) have shown that BrC will absorb some light at wavelengths longer than 405 and have shown a spectral wavelength dependency that can vary approximately between λ^{-2} and $\lambda^{-2.5}$. Hence, the absorption by BrC at 405 nm is 4-7 times larger than at 870 nm. While not zero, the difference is large enough that applying a correction factor will have negligible impact on the final results and conclusions. Following other studies using this method [13,30,31], we assume that the AAE of BC is unity. As such, the AAE was calculated as,

$$\mathrm{AAE}(\lambda_1\lambda_2) = -\frac{ln\left(\frac{\mathrm{b}_{\mathrm{Absorption}\ (\lambda_1)}}{\mathrm{b}_{\mathrm{Absorption}\ (\lambda_2)}}\right)}{ln\left(\frac{\lambda_1}{\lambda_2}\right)} \qquad (1),$$

where $b_{Absorption}$ will be the BC-associated absorption coefficient, λ_1 = 405 nm and λ_2 = 870 nm [29]. While AAE (the left side of the equality) is assumed to be 1 for black carbon, equation (1) can be solved for $b_{Absorption(\lambda_1)}$, with the corresponding value for the wavelengths,

$$\mathrm{b}_{\mathrm{Absorption}\ (405\mathrm{nm})} = (\mathrm{b}_{\mathrm{Absorption}(870\mathrm{nm})})\left(\frac{870\mathrm{nm}}{405\mathrm{nm}}\right) \qquad (2)$$

and subtracted from the output signal of the instrument measuring at λ_1. Using this method, we determined the BrC absorption coefficient for the three seasons characterized in this paper,

$$\mathrm{BrC}_{Absorption} = \mathrm{B}_{\mathrm{Absorption(PAX\ 405\ nm)}} - \mathrm{b}_{\mathrm{Absorption(405nm)}} \quad (3),$$

Although this derivation is generally accepted for the derivation of BrC, it is not without uncertainty because the AAE of BC available in the literature has been observed to fluctuate around the assumed value of 1. Liu et al. [19] specified a range of 0.6 to 1.3 for the AAE of BC, which likely (plus instrumental measurements uncertainties not calculated at present) contributes to the variation we see in the BrC-derived Babs, i.e., a standard deviation about the mean of ±1.38 (Mm^{-1}) for the summer characterization, ±3.69 (Mm^{-1}) for the winter characterization and ±2.09 (Mm^{-1}) for spring. After the BrC is determined from equation (3), what is left is the BC (plus a minor amount of mineral dust) Babs $-\mathrm{b}_{\mathrm{Absorption\ (405nm)}} -$ as detected by the PAX at 405 nm. Equation (2).

2.2.3 Single Scattering Albedo and Absorption Ångstrom Exponent Calculation

The optical thickness of aerosols considers the extinction of the incident radiation without contemplating whether it is produced by absorption or dispersion. The single scattering albedo (SSA) determines the relationship between the extinction due to scattering alone and due to scattering plus absorption. The single scattering albedo is an indicator of the absorbance capacity of an aerosol that depends on its chemical composition, shape and size, taking values between 0 (highly absorbent particles) and 1 (poorly absorbent particles). The PAX defines SSA as,

$$SSA = \frac{Sattering\ Coefficient}{Total\ extinction} = \frac{B_{scat}}{B_{scat} + B_{abs}}$$

Any value less than 1 will indicate that the particle has some light absorbent characteristics, which it is most of the aerosol particles, including BC and BrC. A value much closer to zero will indicate a highly absorbent particle. The El Paso-Ciudad Juarez region suffers from seasonless

dust storms. Though dust and mineral dust particles are said to be negligible from the PAX 405 nm data analysis and optical parameters, they should be nonexistence on the PAX 870 SSA measurements. In January 2022, for the winter season, the values varied between 0.4 and 0.8, with an average of 0.66 ±0.91. May 2022 had the highest SSA values that did not go below 0.88, with several days that showed only scattering coefficient outcomes, with an average 0.96 ±0.03. For the summer season (August and September 2021), the SSA didn't go below 0.65, with an average of 0.79 ±0.06 for the wildfire event days, and 0.83 ±0.06 for baseline or non-event days. These results indicate a lot of light-scattering particles, just BC for PAX 870, maybe due to some external and internal mixing state. We have to remember that BC (and BrC) not only absorb light but also scatter it.

The PAX instruments outputs the SSA as a derived parameter. Since the PAX 870 nm absorption coefficient it is understood to interact mostly with black carbon particle, we have taken its single scattering albedo for seasonal characterization.

The optical thickness depends on the wavelength; it was parameterized by the 1929 Ångstrom's Law, which describes the aerosol size distribution in an integrated column and can be derived from simultaneous optics thickness measurements at various wavelengths, in our case, two. This law is expressed as: $\tau(\lambda) = \beta\lambda^{-\alpha}$

Where τ is the optical thickness at a wavelength λ, measured in micrometers (μm), and α and β are two fit parameters. The parameter α is the Ångstrom exponent, which depends on the aerosol size distribution. According to Wagner and Silva, (2008) [41], this parameter, in theory, takes values from 0 to 4, where the lower values are associated with large particles. The parameter β is the turbidity coefficient and matches the optical thickness of aerosols corresponding to λ = 1 μm. However, the optical thickness of the aerosol is not measured directly but must be estimated from observations of atmospheric spectral transmission. From the Angstrom's Law expressed above, the Absorption Ångstrom Exponent (AAE), takes the form of equation (1), using the PAX instruments' absorption coefficients, for λ_1= 405 nm and λ_2= 870 nm. The analysis for the seasonal values is discussed in each season individually.

Chapter 3: Analysis

3.1 EBC and BrC Winter Season Characterization

We have selected January 2022 as a representative sample for the winter season. As mentioned in section 1.2, we derived an absorption coefficient baseline due to BC and BrC in the El Paso and Ciudad Juarez airshed and determined that this baseline increases each Winter as a result of household heating by burning of wood, charcoal, and other biomasses materials. These alternative heating methods are prompted by the lack of efficient and/or updated centralized heating systems among the poorer areas of Ciudad Juarez. Montoya et al. (2006) [28] found a relationship between Winter's low ambient temperatures and CO emissions in the Ciudad Juarez. They attributed it to malfunctioning gas heaters and biomass burning in the city residences. As CO and BC/BrC have common sources, we adhered to the findings in the Montoya et al. study.

We observed two relevant time-segments in the data, 0:00AM to 3:00 PM and 3:00PM to 24:00PM, local standard time (LST). The first time-segment baseline (Figures 1a), shows two main peaks, one at around 1:00 AM, attributed to nighttime international bridge traffic, and a second peak between 6:00 AM and noon, which corresponds to the normal traffic congestion due to morning commuters and brick kilns starting to operate. In the evening segment we saw a significant increase in the Babs averages (~300%) when compared to the first time-segment. The BC and BrC emitted by household heating (introduced by a fast decrease in temperature)is responsible for this increase (especially in a low PBL situation). Figures 1a and 1b illustrate this trend. The PAX 405 Babs in Figure 2a refers to the Babs due to BC absorption measured by the PAX 405 nm and extrapolated from the measurement according to equation (2). The PAX 870 BC Babs in this graph correspond to the Babs calculated by the PAX 870 nm. Each data point on Figure 1 represents a 10-minute average of the measurements. The error bars express the standard error of each averaged data point. The average and maximum values for each peak are displayed in Table 1. The $B_{abs\text{-}BrC}$ averaged of 50% (±20%) of the total Babs as measured by the PAX 405 nm. Figures 2c and 2d present boxplots; 2c shows the data spread for the significant segment,

3:00PM to Midnight. We can see that the spread from the median point is large. Figure 2d shows the total Babs spread, for the whole month, with quite a substantial spread from the median.

Figure 3 displays the CO detected by the TCEQ instruments (CAM41-Chamizal) which are located slightly more than 8 km from our instruments. The three main peaks correspond to the Babs peaks for the same time interval. The most prominent peak, between 3:00 PM and midnight, is around 160% greater than the mid-morning peak and ~180% greater than the early morning peak. A temperature color-coding has been added for temperature reference. The graph shows that, after 4:00 PM, the temperatures start to decrease, and the CO concentrations start to increase. This agrees with our findings that the Babs due to BC and BrC also increase in the late evening hours. The graph has a smoothing filter applied (binomial smoothing filter by Wave Metrics Igor Pro 8 platform). The error bars represent the standard error for each averaged point. As mentioned above, the measurements of CO for the same period, in parts per million (PPM) by volume, display the same general tendency of the Babs that we measured [32]. The authors claim that the behavior of the two graphs, Figure 2a and 2b, and Figure 3, show a correspondence as the sources of carbon monoxide and black/brown carbon are similar.

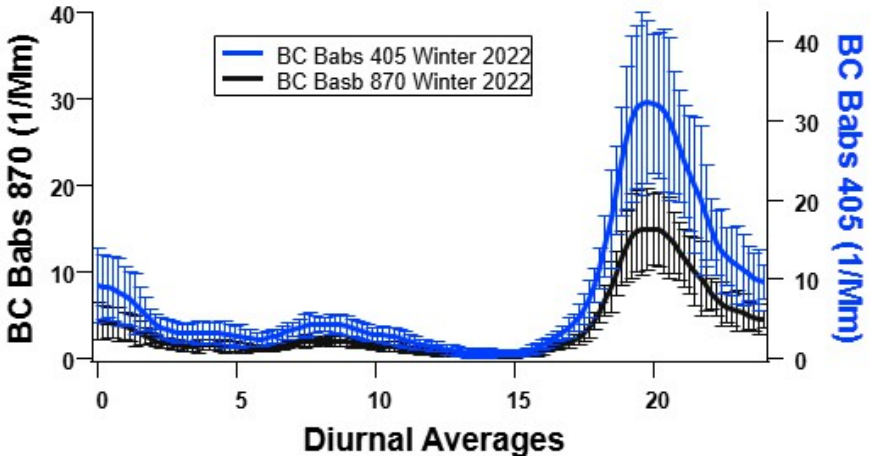

1a

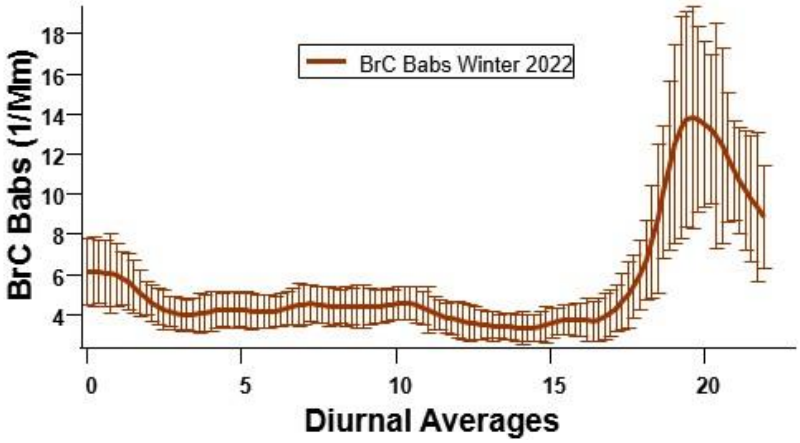

1b

Figure 1: The absorption coefficient, Babs, for January 2021, corresponding to the winter season characterization. 1a compares the Babs due to EBC from PAX 870 nm (left) and PAX 405 nm (right, blue). After 3:00 PM a clear increase in the Babs (~300% increment) is observed in both instruments. We concluded that this increment from its baseline (before 3:00 PM) was related to a decrease in ambient temperature. 1b shows the extrapolated BrC Babs that manifested the same behavior. The standard error was calculated for each data point (10 minutes of observation) and a binomial smoothing filter was applied.

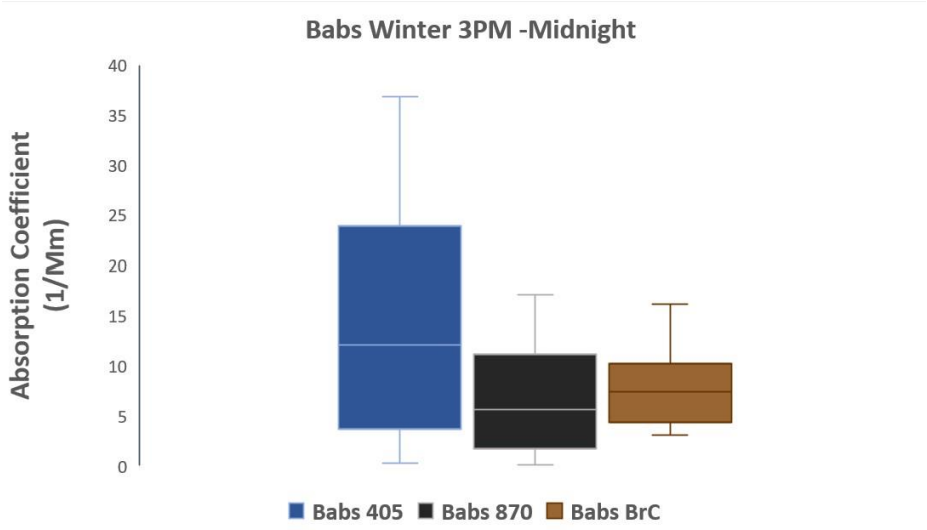

2a

2b

Figure 2: PAX 870 nm, PAX 405 nm, and BrC Babs boxplots that show the spread of the data points. 2a presents the spread for the significant peak after 3:00PM for the EBC Babs of both instruments and for the extrapolated BrC Babs. 2b shows the general spread of the whole month of January for the three optical parameters indicated.

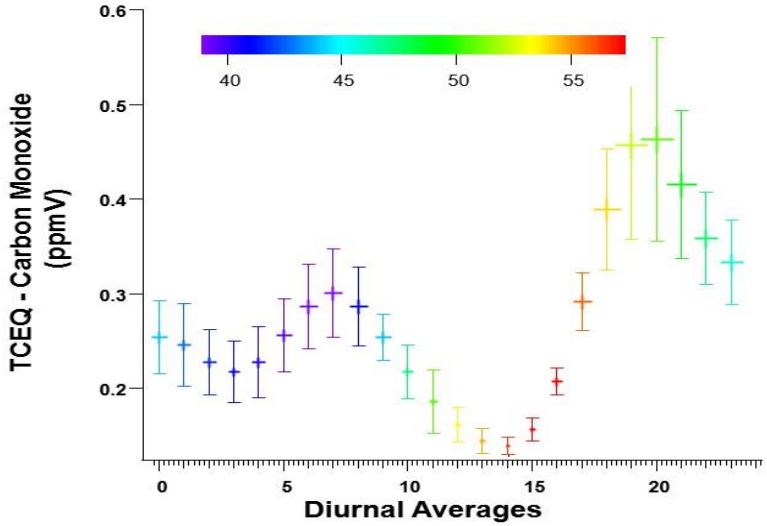

Figure 3: Carbon monoxide molar mixing ratios in parts per million by volume diurnally averaged over January 2022 data from the Texas Commission on Environmental Quality monitoring station at Chamizal National Park, CAM41. The graph has been temperature coded, with the lowest temperatures toward the blue-purple ends and higher temperatures toward the orange red. After 4:00 PM the temperatures start to decrease, and the CO concentration increases.

Table 1: The average and maximum values of the BC and BrC Babs (Babs, Mm^{-1}) for \the three prominent peaks in Figures 2a, 2b, and 3.

Parameter	First Peak		Second Peak		Third Peak (3:00 PM - Midnight)	
BC Babs PAX 405 nm (1/Mm)	4.858 avg.	7.576max.	3.290 avg.	4.440 max.	14.125 Avg.	32.244 max.
BC Babs PAX 870 nm (1/Mm)	2.196 avg.	3.527max.	1.521 avg.	2.067 max.	6.701 avg.	15.010 max.`
BrC Babs (1/Mm)	5.302 avg.	6.109 max.	4.313 avg.	4.582 max.	8.049 avg.	13.810 max
CO-TCEQ (ppm)	0.236 avg.	0.254 max.	0.231 avg.	0.300 max.	0.0341 avg.	0.462 max.

3.1.1 Single Scattering Albedo and the Ångstrom Exponent for the Winter Season

The Single Scattering Albedo (SSA), Figure 4, was calculated using the PAX 870 nm (scattering coefficient divided by the extinction coefficient) for January 2022. Values closer to 1 mean that the particles' extinction was mainly due to scattering. In contrast, a value nearer to 0 denotes that the particles' extinction was primarily due to absorption. The first week of the month showed highly absorbent BC particles, with the minimum value at 0.45. The highest values were less than 0.80. The winter SSA exhibited a stronger absorption coefficient in the aerosol particles, BC in this case, especially when compared to the spring season values. The average value for January was 0.66 ±0.91, an SSA indicating strong absorption that, we believe is due to the ubiquitous black carbon particles present in the atmosphere [34]. Since the PAX was connected to a thermal denuder at a fairly high temperatures, only the SSA of thermally stable particles (or thermally stable particles residues) was obtained. The PAX 870 nm SSA is dominated by BC.

The Absorption Ångstrom Exponent (AAE), from equation (1), $\lambda_1 = 415$ nm and $\lambda_2 = 860$ nm, was calculated using the Babs obtained from the PAX 405 nm and 870 nm for the month of January of 2021 (Figure 5). The average AE for the month was 2.15 ±0.68. The minimum AAE where around January 5 and January 24, with a minimum value of 1.461, whereas the maximum value was around the 19 of January, 3.81. As mentioned in section 2.2.3, this parameter, in theory, takes values from 0 to 4, where the lower values are associated with larger particles [41].

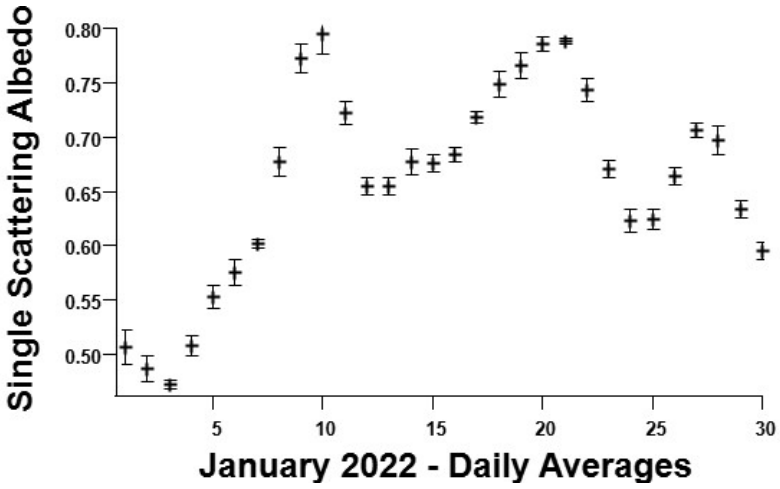

Figure 4: Daily averages of the single scattering albedo were calculated for January 2022 from the absorption and scattering coefficients due to EBC detected by the PAX 870 nm. The graph has a smoothing filter applied (binomial smoothing by Wave Metrics Igor Pro 8 platform). Each point represents a daily average, and the errors are the standard error associated with each point.

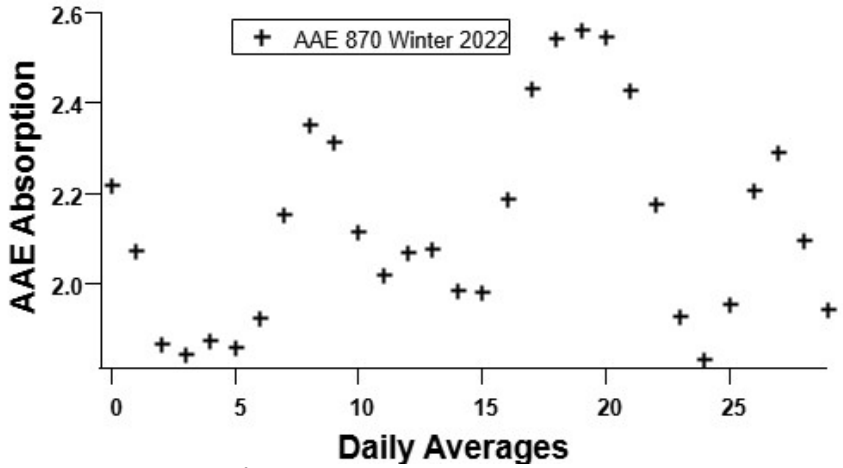

Figure 5: The absorption Ångstrom Exponent -Equation (1)- was calculated using the Babs at 405 nm and 870 nm with the data obtained by the PAX instruments. The values represent daily averages for the month of January, 2022. A binomial smoothing was applied (IGOR Pro 8) to show the shape of the data.

3.2 EBC AND BRC SPRING SEASON CHARACTERIZATION

For characterization completeness, we decided to present what a "normal" season looked like. We say "normal" as no especial cold weather nor wildfire events, were detected. We chose May of 2022 (28 days of data) as a month to denote the spring season. In Figure 6, we present the absorption coefficient due to EBC for both instruments. In this month, the highest peak was at around 7:30AM. The EBC calculated for the PAX 405 nm had an average of 2.99 ±1.66 (1/Mm), with a maximum value of 7.428 (1/Mm) at 7:23AM. For the PAX 870 nm, the average was 1.39 ±0.77 and a maximum of 3.23 at around the same time. The graph doesn't show a particular trend per se as there were many peaks and valleys on the data, with values varying between 0 - 7 (1/Mm) for the 405 PAX and 0-3 (1/Mm) for the 870 PAX , which doesn't infer a significant variation. Guided by the graph, of notice is the peak at around 7:30 AM and the trough at around 6:45 PM. As mentioned at the beginning of this section, this data was not affected by the temperature dependency we saw in the winter season, neither by wildfires, which were predominant in summer changes, hence, spring should reflect a baseline behavior: BC and BrC produced by incomplete engine combustion for the heavy truck and commercial/particular vehicles in the bridges, and the inefficient combustion of the fires used by the brick kilns.

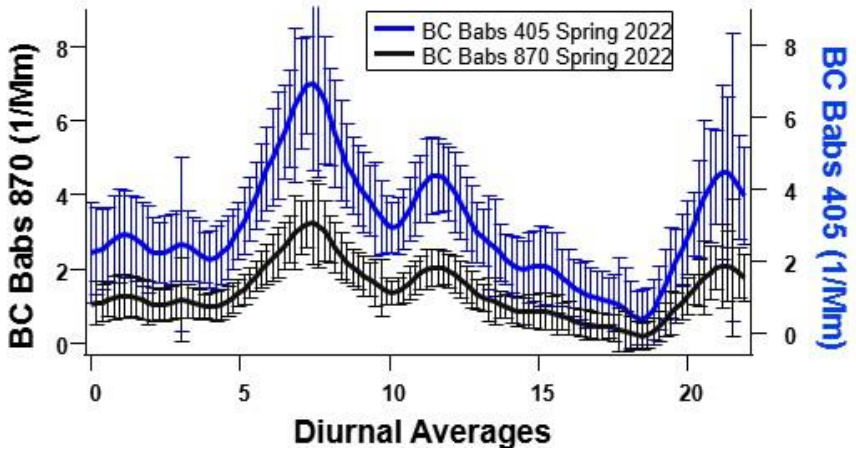

Figure 6: EBC Babs for 28 days of May, 2022. On the vertical axis, the absorption coefficient (units of inverse length), for the PAX 870 nm on the left, and 405 nm on the right (blue). The x-axis shows the diurnal averages for the 28 days of data (from midnight to midnight). Each point represents 10 minutes of observation plus the standard error for each 10-min point, and the graph has a binomial smoothing filter applied.

The brown carbon absorption coefficient for the month is summarized in Figure 7. Equation (3) indicates that BrC Babs is an extrapolated information derived from equation (1). The average for the 28 days came up to 5 ±1.4 (1/Mm), with a maximum and minimum values of 7.6 and 1.8 (1/Mm). Since the BrC Babs are extracted from the PAX 405 nm Babs, we determined that 65.30% of the total Babs across 405 nm wavelength, as calculated by the instrument, correspond to the Babs of brown carbon. This percentage is indeed a good depiction of the ratios of BrC/BC Babs for baseline data, which turned out to be a higher proportion when compared to the BrC/BC for the winter season and the wildfire event days of summer.

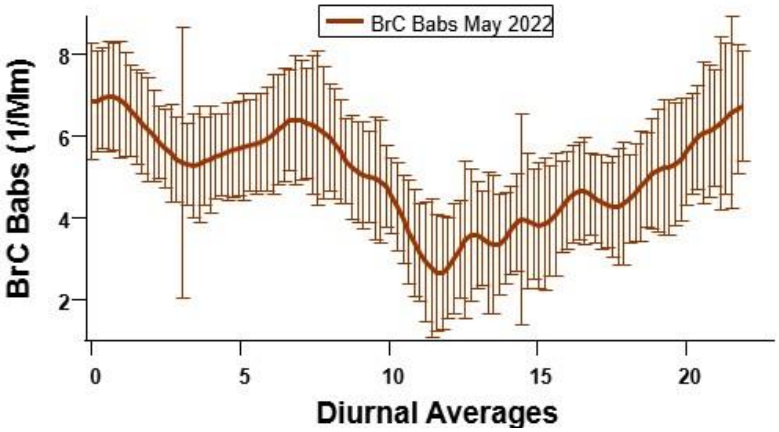

Figure 7: the absorption coefficient due to brown carbon, diurnal averages, for 28 days of May, 2022. The peaks and valleys are a representation of the BrC Babs emitted by the vehicles, commercial and particular, waiting to cross the border between El Paso and Ciudad Juarez, and also by the BrC emitted by the brick kiln common of Ciudad Juarez. Each point represents 10 minutes of observation plus, the standard error for each 10-min point. The graph has a binomial smoothing filter applied.

In the boxplot of Figure 8, we compared the EBC Babs as measured and derived from the two instruments. The boxplot shows the spreading of the data, with high variation in the collected values. For a visual inspection, the BC Babs from PAX 405 nm, correspond to the Babs of PAX 870 nm time the wavelength ration (870/405), and the BrC Babs are what is left of the PAX 405 nm Babs after subtracting the BC Babs from PAX 405 nm.

For completeness, we have added the TCEQ carbon monoxide (Figure 9), temperature-coded, collected from CAM41, in Chamizal National Park, El Paso, TX. Not a big fluctuation in carbon monoxide for spring -0.10 to 0.30 ppmV-, which is to be expected for a season not affected by either extreme temperature nor predominant external $PM_{2.5}$ contributions. With an average of 0.15 (ppmV), and a maximum value of 0.27 (ppmV) at around 9:00 PM., the temperature variation toward the late evening somewhat paralleled the increment in the CO concentration, but not significantly.

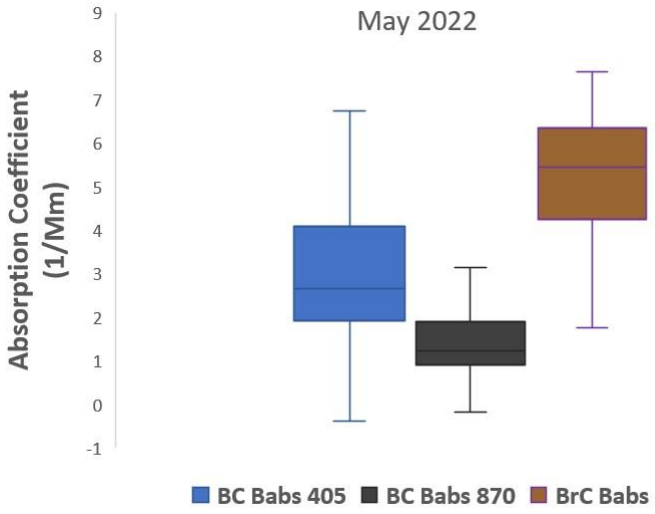

Figure 8: A boxplot presenting the spreading of the data, from a median value. The BC Babs 405 (blue) presented the highest spreading of the data values.

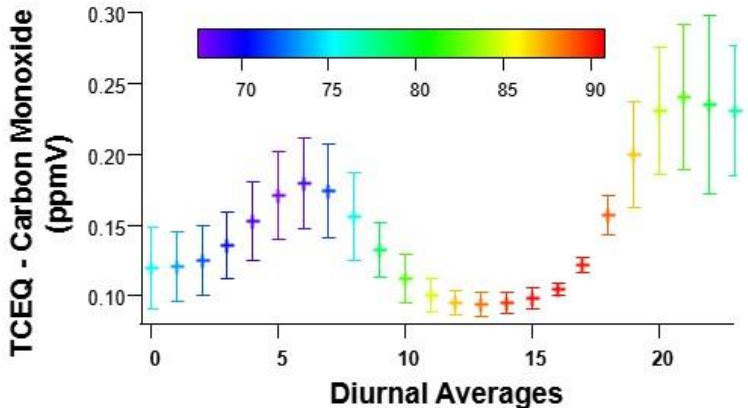

Figure 9: The Carbon Monoxide diurnal averages (24-hour period) as detected by the Texas Commission on Environmental Quality, Chamizal National Park, Cam41. The units are parts per million by volume, ppmV, with values between 0.10 and 0.30, the values are temperature-coded, with red indicating the highest temperature (here around 90ºF), and purple, the lowest (around 70ºF).

3.2.1 The Single Scattering Albedo (SSA) and the Absorption Ångstrom Exponent for the Spring Season

The SSA and AAE were taken directly from the derived measurements done by the PAX 870 nm instrument. The SSA average May of 2022 (Figure 10), was 0.96 ±0.03. As said before, this ratio narrates the scatter coefficient and the extinction coefficient. For a month where extreme observations were absent, the particles of BC demonstrated their capability to scatter light perfectly. Most of the days showed SSA greater than 0.92, which means that the absorption coefficient captured for these particles was minimal. As the PAX 870 nm has been dedicated to the study of BC exclusively, these values are all corresponding to the BC particles characteristic. As discussed by Cheng et al. [42], BC particles are understood to be dominant absorber as external coating and internal mixing, due to the aging process, tends to increase their absorbing properties. However, as their article discusses, these coating and internal mixing effects on scattering are not well understood and show a solar radiance angular dependency.

The Absorption Ångstrom Exponent (AAE), from equation (1), $\lambda_1 = 415$ nm and $\lambda_2 = 860$ nm, was calculated using the Babs obtained from the PAX 405 nm and 870 nm for 28 days on May, 2022 (Figure 11). The average AE for the month was 2.167 ±0.283. The lowest AAE, bellow 2.0, were around May 8 and May 15, with a minimum value of 1.904 on May 13, while the higher values were observed after May 17, with a maximum value of 2.857. As mentioned in section 2.2.3, this parameter, in theory, takes values from 0 to 4, where the lower values are associated with larger particles [41].

When comparing Figures 10 and 11, we were able to see a clear decrease of both optical parameters toward the 10 of the months, and a strong increase toward the 15. As AAE is commonly

accepted to be inversely proportional to a particle's size, one could assume the presence of much bigger (externally and internally mixed) and absorbent BC particles in correspondence with Cheng et al. conclusions [42].

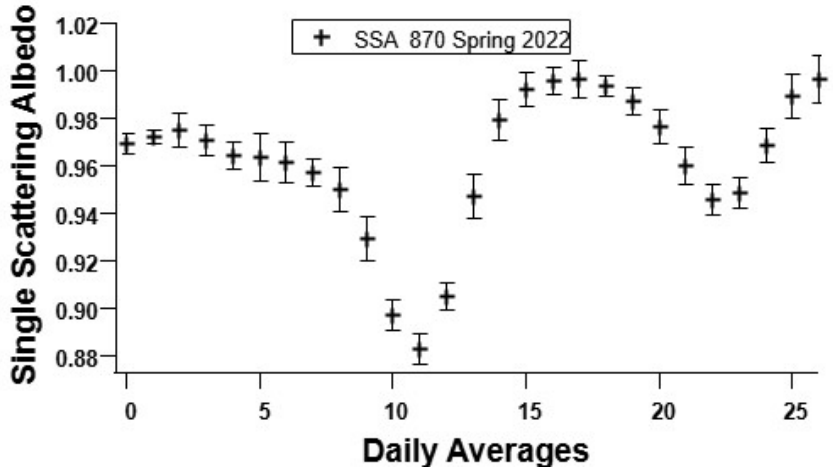

Figure 10: The single scattering albedo for 28 days of May, 2022, as measured by the PAX 870 nm. The x-axis shows daily averages of the parameter displayed on the y-axis. Between the 5th and 15th of the month, the values showed a prominent decline, maybe related to the mixing and coating of the BC particles. The graph had a binomial smoothing filter applied.

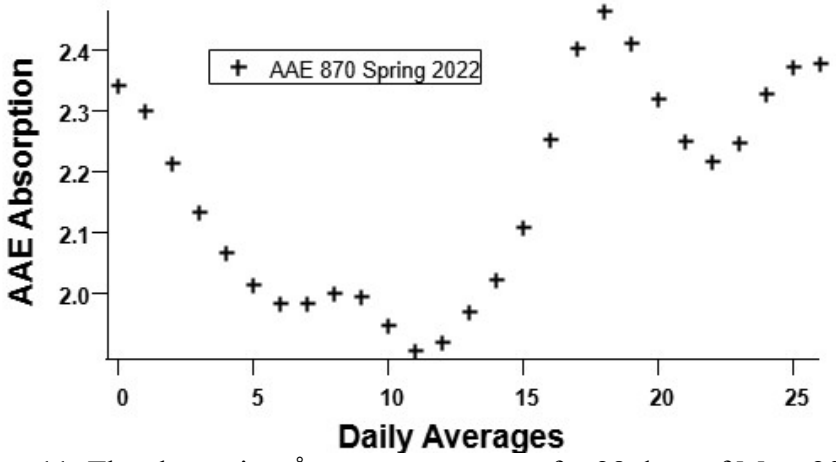

Figure 11: The absorption Ångstrom exponent for 28 days of May, 2022, as measured by the PAX 870 nm. The first 15 days of the month were characterized by an increase in particles' size, which started to decrease on the second half. The graph had a binomial smoothing filter applied.

3.3 EBC AND BRC SUMMER WILDFIRE SEASONAL CHARACTERIZATION

An important objective of our study was to identify wildfires aerosol influences in the El Paso – Ciudad Juarez region. The first step was to establish the baseline (as defined in section 1.2) of the Babs for the period. Figure 12 compares these baselines as measured by both instruments. Here, we still see the two main peaks, where the third peak, in the early morning hours, is almost non-existent (compared to Figure 1a for example, where we still notice the early hours peak), which were driven by the heavy traffic at peak hours, and the operation of the brick kilns. The Summer baseline Babs had the same sources as the other seasons' baselines. We observed non-periodical but obvious increments from the baseline during the summer season and conclude that such increments were due to wildfire smoke.

We ran two different models to show that the US West Coast wildfire plumes reached the El Paso – Ciudad Juarez airshed. One of these models was the High-Resolution Rapid Refresh (HRRR). The HRRR model maps showed that the west coast wildfire plumes usually travel in a North-East direction, later moving southward into our region. Then, with the help of the HYSPLIT, 72 hours backward trajectory, we confirmed that the wind direction presented by the model, supported what the HRRR model indicated.

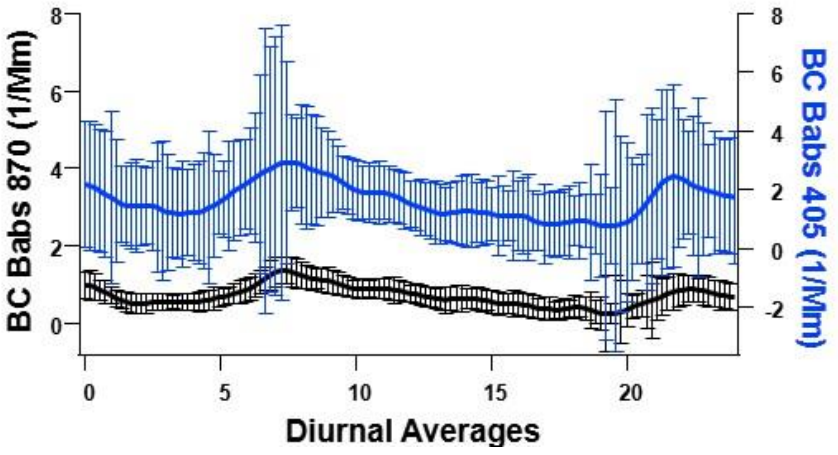

Figure 12: The baseline diurnal averages of the Babs for August and September of 2021. In black (left y-axis), the baseline as measured by PAX 870 nm with its highest peak of 1.003 1/Mm at around midnight and its lowest point of 0.6639 1/Mm at around 3:30 PM (local times). In blue (right y-axis), the baseline as measured by PAX 405 nm with its highest peak of 7.658 1/Mm at around 7:30 AM and lowest values of 3.860 1/Mm at around 3:30 PM. The graph has a smoothing filter applied (binomial smoothing by Wave Metrics Igor Pro 8 platform). The errors bars represent the standard error associated with each point.

Using the HRRR and HYSPLIT models we recorded the days when the wind direction and plume trajectories were transporting smoke plume particles to our region and labeled them Event Days. Thus, for August-September 2021, we encountered eighteen such events, listed in Table 2, along with the location of the wildfires from where these air masses originated. The HRRR product is a map with the smoke near the surface (3 km) reported as a mass concentration in units of $\mu g/m^3$.

Table 2: The August and September event days where the smoke plumes output by a wildfire made their way to our region. The California wildfires were mainly in the north part of the state. The HRRR reported the plumes as $PM_{2.5}$ in micrograms per cubic meter through a color-coded volume. Most of the fires lasted for a couple of days.

Event Day	Smoke Source State	Event Day	Smoke Source State
08/06/21	CA/NV	09/08/21	CA/OR
08/07/21	CA	09/09/21	OR/ID/MT
08/17/21	CA/NV	09/10/21	OR/ID/MT
08/18/21	CA	09/11/21	NV/ID
08/20/21	CA	09/13/21	CA
09/02/21	CA/NV/ID	09/14/21	CA
09/03/21	CA/NV/ID	09/16/21	CA
09/06/21	CA/OR	09/17/21	CA
09/07/21	CA/OR/ID	09/18/21	CA/MT

We have used two months of observation, summarized in Figure 13. This graph contains the daily averages of the surface mass concentration due to EBC as derived from the Babs measured by the PAX 870 nm -Equation (4). The bold markings are the event days' averages. The graph covers from 1 August first to 23 September 2021. The event days have an average of

higher EBC mass than a non-event day (light marking, baseline). We compared a non-event day to an event day and determined that the wildfire plumes' EBC mass surface concentration was 58% - 63% larger than the baseline EBC mass concentration.

The mass concentration the PAX 405 nm calculates includes EBC, BrC, and some mineral dust. However, this is not the case for the PAX 870 nm since most of the Babs is due to BC at that wavelength. The derivation of the mass concentration from the PAX 870 nm measured Babs (equation (4)) uses the Babs and a fixed absorption cross-section (equation (5)), as suggested by Bond et. al (2006) [21] and corrected for wavelength.

$$\text{BC Mass}\left(\frac{\mu g}{m^3}\right) = \frac{B_{abs}\left(\frac{1}{Mm}\right)}{\text{BC MAC}\left(\frac{m^2}{g}\right)} \qquad (4)$$

$$\text{BC MAC} = 7.5\ \left(\frac{m^2}{g}\right) * \left(\frac{550\ nm}{870\ nm}\right) = 4.74\ m^2/g \qquad (5),$$

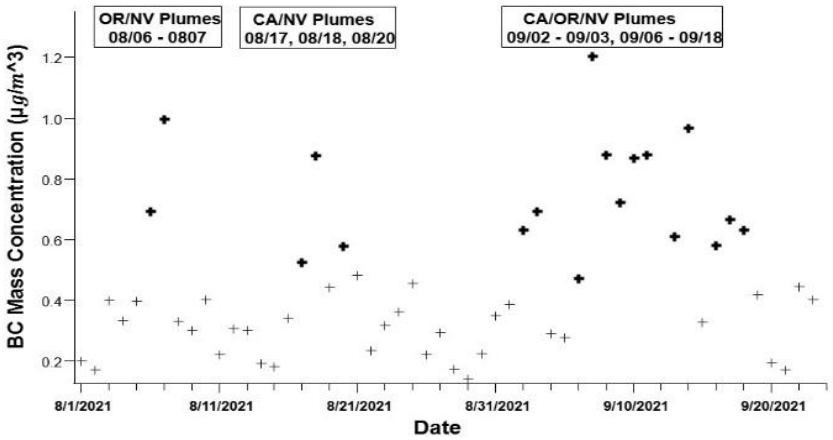

Figure 13: Equivalent Black Carbon mass concentration measured in micrograms per cubic meter. The bold marking represents those eighteen event days when the wildfire plumes reached our instruments.

Figure 14 presents the trends in the summer wildfire (WFE) Babs due to EBC measured with the PAX 870, that had an average value of 2.9 ± 1.8 (Mm^{-1}), and the Babs due to EBC and

a small amount of mineral dust as derived from the PAX 405 nm with an average of 11.4 ± 4.9 (Mm^{-1}). The trends in the baselines are still present in the seasonal behavior and explains the peaks observed in the figure. However, the three main peaks typical of the background Babs were reduced to two peaks. The error bars represent the standard error associated with each averaged point. The BrC Babs average for event days (Figure 15a) was 5.2 ± 1.7 (Mm^{-1}) and 3.8 ± 0.76 (Mm^{-1}) for non-event days. Evaluating the portion of the Babs from the PAX 405 nm that corresponds to BrC Babs is an innovation for our region. The percentage of the Babs due to BrC from the Babs calculated by PAX 405 nm was 53 ± 7% for event days. We conclude that at a wavelength of 405 nm, about 50% of the light absorption by particles during wildfire events is due to non-volatile BrC particles. This graph shows a large number of fluctuations but the standard deviations are also large. Though we did not separate the BrC Babs from the baseline graph in Figure 15, one must assume that there are background BrC particles in the region, independent of the wildfires' smoke coming from the West of the US. Figure 15b presents the spread, boxplot, of the BrC data for three random event days, September 3, September 14, and September 16 as measured by the PAX 870. Figure 14c shows the boxplot data spreading as measured by the PAX 405.

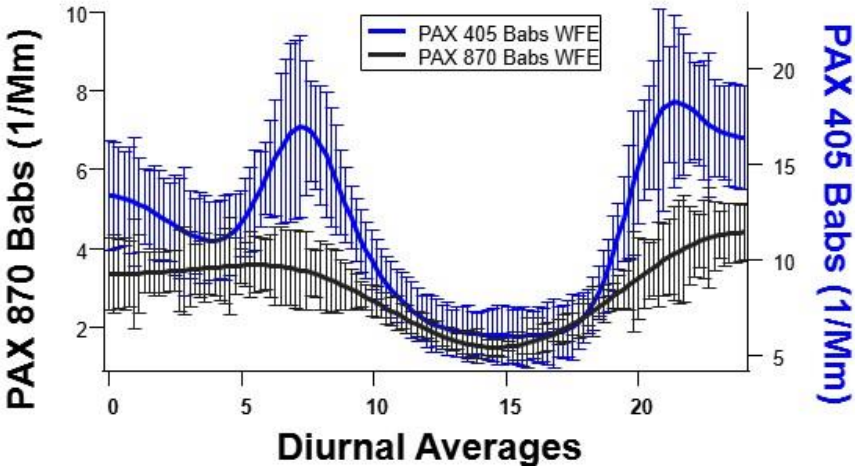

14a

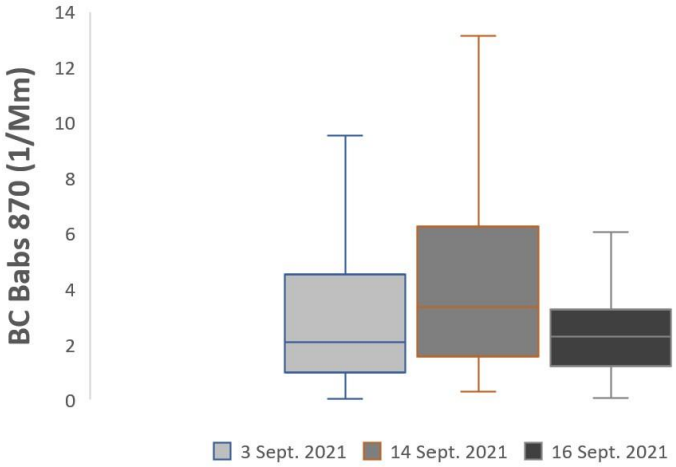

14b

14c

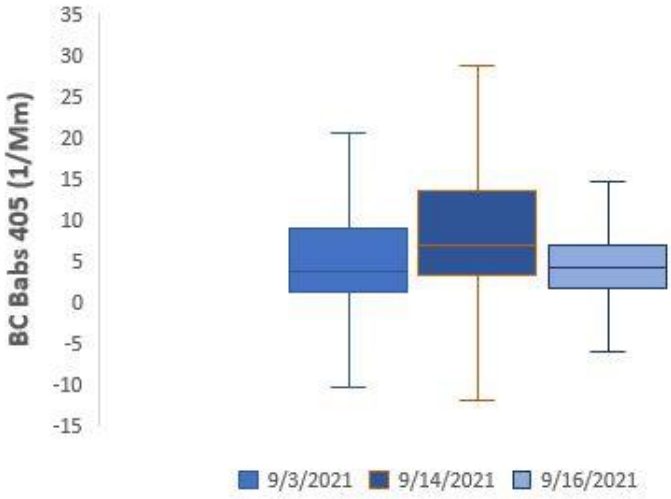

Figure 14: (a) shows the diurnal averages of the Babs due to BC particles of the eighteen wildfire event days of the season. The values on the left y-axis (in black) of the graph were reported by the PAX 870 nm, and on the right y-axis (blue) were calculated from the 405 nm PAX. The graph has a binomial smoothing filter applied. The error bars in (a) represent the standard error associated with each averaged point. Boxplots were added to present the spread of the data over 10 minutes averages for three California wildfire event days, September 03, September 14, and September 16. (b) shows the data spread for the BC Babs PAX 870 nm while (c) shows the spread of the BC Babs calculated from the PAX 405 nm.

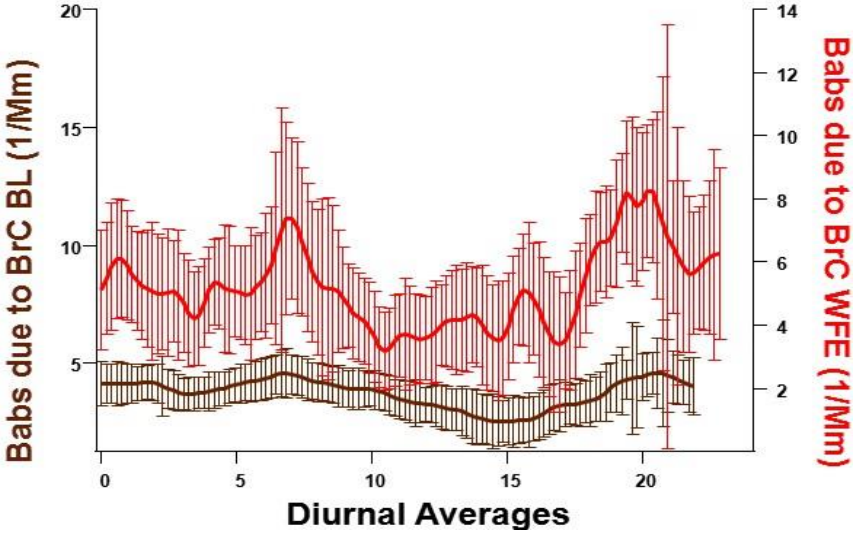
Babs due to BrC BL (1/Mm)
Babs due to BrC WFE (1/Mm)
Diurnal Averages
20
15
10
5
0
5
10
15
20
14
12
10
8
6
4
2

15a

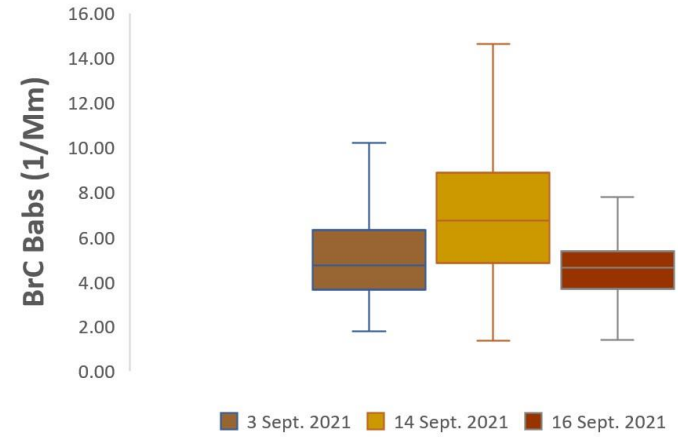
BrC Babs (1/Mm)
16.00
14.00
12.00
10.00
8.00
6.00
4.00
2.00
0.00
3 Sept. 2021
14 Sept. 2021
16 Sept. 2021

15b

Figure 15: (a) The inferred BrC Babs is graphed here for the diurnal averages of 1 August through 23 September 2021. The Babs displayed in red are due to BrC corresponding to the eighteen event days (BrC Babs WFE), and displayed in black is the baseline (BL), BrC Babs driven by pollution from vehicular traffic. The peaks agree with the costumery rush hour times.
The graph has a smoothing filter applied. The error bars represent the standard error associated with each averaged point. (b) represents the spread of this data for three California wildfires event days.

3.3.1 The Single Scattering Albedo (SSA) and the Absorption Ångstrom Exponent for the Summer Wildfire Season

We reported the SSA over August and September of 2021 derived from the 870 nm PAX; the event days were denoted in bold black markers as shown in Figure 16. The average SSA value for August-September was 0.83 ± 0.06, and the SSA calculated over the event days was 0.79 ± 0.06. The event days resulted in a smaller SSA value which was to be expected as the wildfires introduced many more absorbing BC particles than the baseline, local sources.

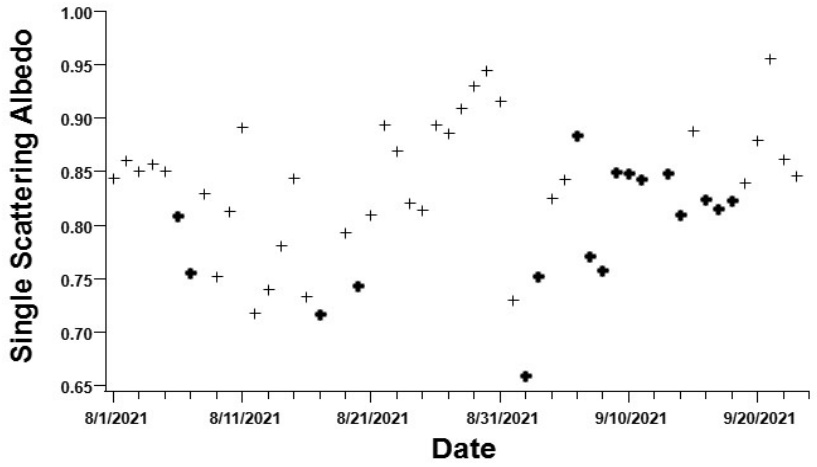

Figure 16: The Single Scattering Albedo (SSA) for September of 2021 was calculated using the PAX 870 instrument. The bold marking indicates the SSA of event days. Each point represents the average measurement for the day.

From the Absorption Ångstrom Exponent equation (1), the AAE for the Summer Wildfire Event Days and non-Event are shown on Figure 17. As observed in the figure, the AAE for the Summer Wildfire Event Days decreases, this is because the BC AAE becomes smaller in the summer season during a wildfire event, in particular for particles with mean diameters larger than 0.12 micrometers, which is symptomatic that the BC particles that arrive in the El Paso region are aged [18, 19]. The average value for the baseline AAE for the period was 3.12±1.4. The average value for the eighteen days when wildfire smoke was detected (plus the background or baseline AAE for those days) was 1.81±0.20.

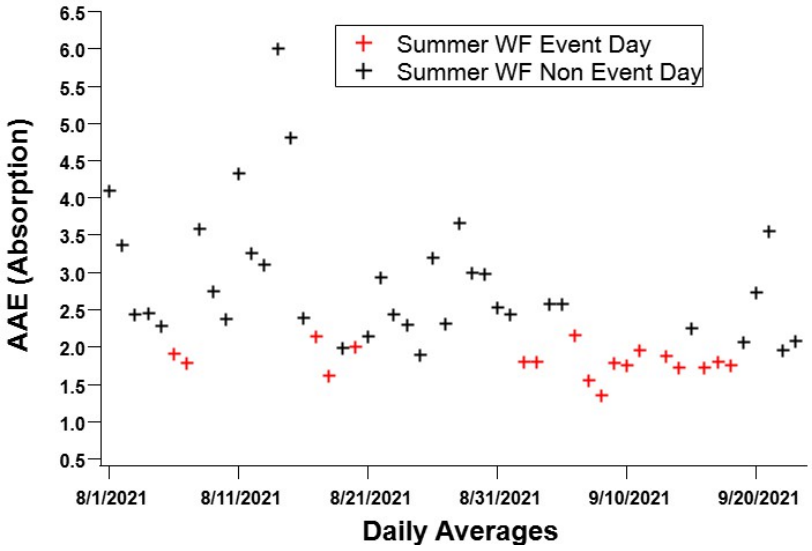

Figure 17: The Absorption Ångstrom Exponent was calculated using the Babs as calculated by the PAX instruments at 405 nm and 870 nm. The black markings correspond to the daily averages of the days where no wildfire smoke arrived at the region and therefore represent the AAE for the basline. The red markings indicate the daily averages for the days when wildfire smoke was detected in the region - event days- (eighteen event days between August and September of 2021). The baseline AAE was not subtracted from the event days AAE, hence, the red markings indicate the AAE for the event days plus the background AAE.

3.3.2 HRRR and HYSPLIT for the Wildfire Event Days

Smoke from the wildfires tends to travel long distances from the source via long-distance transport, affecting local air quality in downwind areas. The HRRR wildfire smoke maps (Figure 18 (a) and 19 (a)) were evaluated for each event day and show the wildfire origin and smoke cloud dispersion. We consider it an event day when the model-simulated smoke plumes arrived at the El Paso-Ciudad Juarez airshed. The HRRR map shows a high $PM_{2.5}$ surface mass concentration in the states to the northwest of the area under study. As per the color scale of the HRRR map, El Paso received an average of 2-8 $\mu g\ m^{-3}$ of $PM_{2.5}$ during the event days. The HYSPLIT air parcel trajectory report is shown in Figures 18 (b) and 19 (b), and each graph contains 72-hour backward trajectories from the study location (UTEP), with a new trajectory every 6 hours. The HYSPLIT trajectories ensured that the air masses arriving in the study area could be associated with a region with high levels of wildfire smoke. The source of air masses was identified by visually inspecting the HRRR maps showing high concentrations of smoke and HYSPLIT backward trajectories. Figure 12 (b) depicts a backward trajectory (light blue) that began on 6 September, 2021, at around 4 km (free troposphere) above ground level and descended to about 1 km (within the PBL) as it approached the study region on 9 September 2021. The HRRR map for 8 September 2021, shows significant concentrations of wildfire smoke in those states.

Similarly, as shown in Figure 19 (b), two 72 hours backward trajectories, light blue and red, from 7 September 2021, at the height of around 4 and 3 km, respectively, descended to lower elevations as they approached the El Paso region. So, based on these backward trajectories, the smoke detected by the instruments (both UTEP and TCEQ CAMS) was associated with air masses from western and northwestern US states.

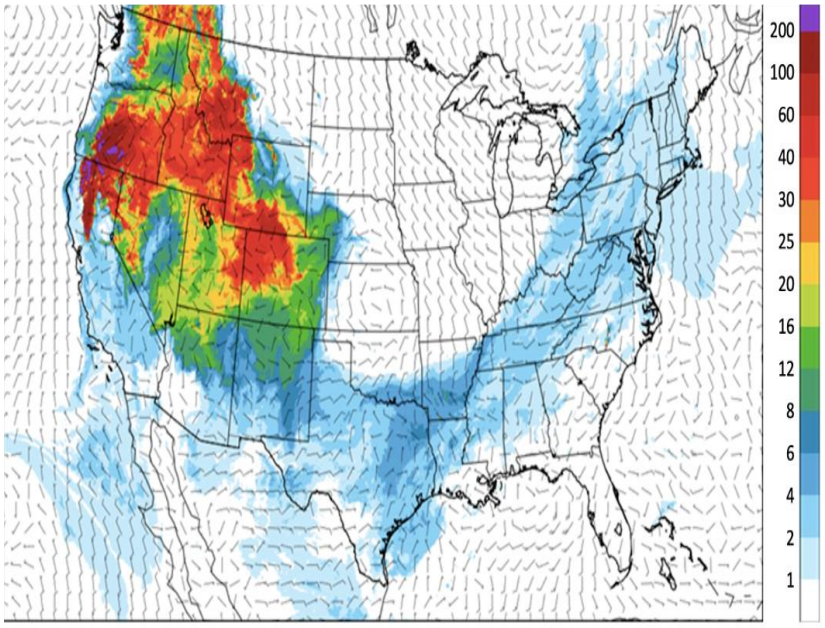
200
100
60
40
30
25
20
16
12
8
6
4
2
1

18a

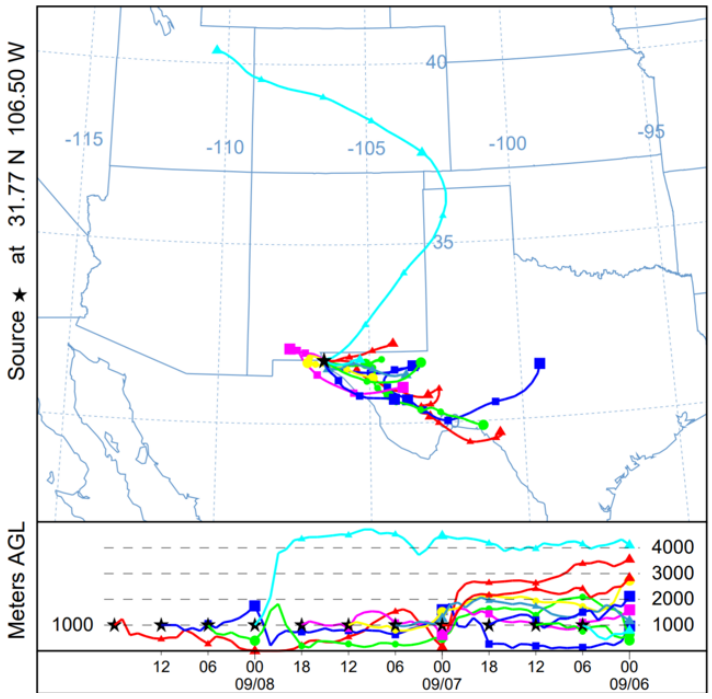
Source ★ at 31.77 N 106.50 W
-115
-110
-105
-100
-95
40
35
Meters AGL
1000
4000
3000
2000
1000
12
06
00
18
12
06
00
18
12
06
00
09/08
09/07
09/06

18b

Figure 18: The HRRR and HYSPLIT analyses for 8 September 2021. (a) The HRRR map indicates the surface mass concentration, from purple at the origin of the wildfire (northern California and south Oregon) to light blue at its lowest concentrations. El Paso, located at the western corner of the state of Texas received 2-8 micrograms per cubic meter of $PM_{2.5}$. (b) The HYSPLIT backward trajectories run for 72 hours at height 1, 1.5 and 2 km from the surface.

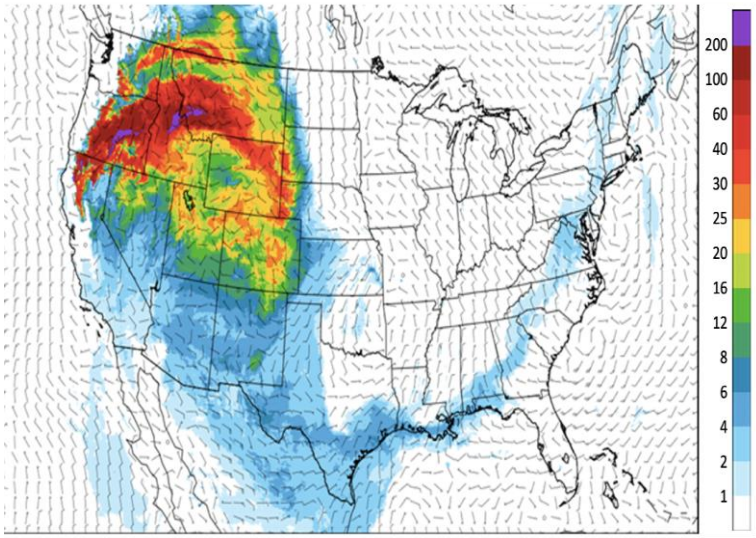

19a

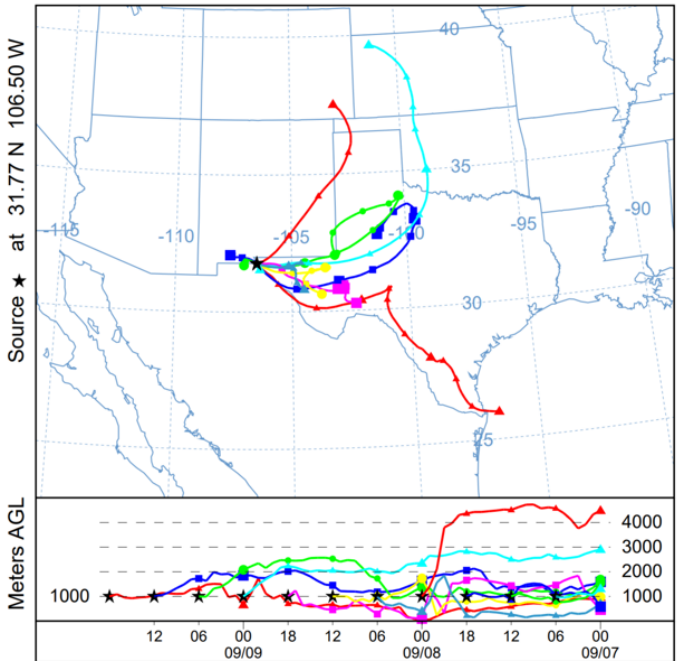

19b

Figure 19**:** The HRRR and HYSPLIT analyses for 9 September 2021. (a) The HRRR map indicates the surface mass concentration, from purple at the origin of the wildfire (northern California and south Oregon) to light blue at its lowest concentrations. El Paso, located at the western corner of the state of Texas received 2-8 micrograms per cubic meter of $PM_{2.5}$. (b) The HYSPLIT backward trajectories run for 72 hours at height 1, 1.5 and 2 km from the surface.

3.3.3 Composite Synoptic Conditions and PBL Structure during the Wildfire Exceedance Events

Synoptic conditions play a significant role in pollution accumulation and its dispersion in the El Paso Juarez region [2,3,37]. Smoke particles in the free troposphere could be transported to lower altitudes by synoptic subsidence and potentially enter the PBL through an entrainment process. Subsequently, turbulence within the PBL mixes these smoke particles, resulting in higher pollutant concentrations recorded by the ground stations. The BC and BrC exceedance episodes locally observed due to wildfires in the north and northwestern states can be linked to two unique synoptic situations during the study period. The first situation was distinguished by a high-pressure system over and to the north-northwest of the study region, which resulted in a stable atmospheric condition and shallow PBLHs. This stable condition is the most common and favorable synoptic scenario linked with severe pollution episodes in the region during the summer months [38]. The circulations linked with the formation and presence of hurricane Olaf near the south of Baja California were the second synoptic scenario during the study period. The stagnant conditions caused by the lower PBLHs, and calm surface winds associated with these synoptic conditions resulted in high EBC concentration levels in this area.

The composite synoptic maps were obtained from NOAA's National Weather Prediction Center (WPC) for each of the above-described synoptic situations during the EBC exceedance days. Figure 20 (left) shows the presence of a high-pressure system over the study area leading to stable atmospheric conditions and sinking motion resulting in suppression of the PBL growth. Also, in Figure 20, we observe the stable conditions prevalent over the south of New Mexico and

west and Southwest of Texas due to the presence of hurricane Olaf near the southern tip of Baja California. The high-pressure system in the north and northwest and the low-pressure system (hurricane Olaf) in the Southwest gave rise to circulation patterns both on the surface and aloft, as seen in Figures 18 and 19, carrying the wildfire smoke to this region.

Backscatter profiles for 6 and 7 September 2001 obtained from the Vaisala ceilometer can be seen in Figure 21. A strong backscattered intensity (green profile) indicating the significant presence of particles was observed. The PBLHs are indicated by the dark green dots in the figure. The black dots around 2 am LST on 6 September are cloud base heights. The residual layer of 5 and 06 September 2021 was deeper (1 km and 2 km, respectively) than the convective boundary layer on the following days, i.e., 6 and 7 September 2021. On September 6, the convective boundary layer merged with the deep residual layer shortly after it formed around 6 am. Compared to September 6, when the maximum daytime PBLH can be visually observed around 1.5 km, the PBL appeared to be shallow (maximum daytime height around 0.75 km) on 7 September, impacting the local air quality.. This daily variation in the PBLH was mainly attributed to the high-pressure region over the study area, as already pointed out in Figure 20.

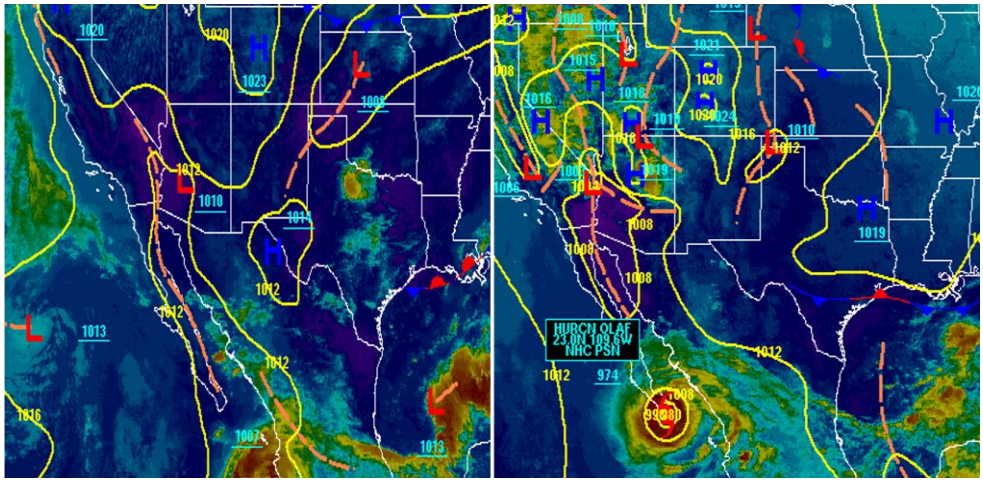

Figure 20: The satellite composite of 7 September 2021, at 1500Z showing the presence of a high-pressure system over the study area (left), and 10 September 2021, at 03Z showing hurricane Olaf near the southern coast of Baja California.

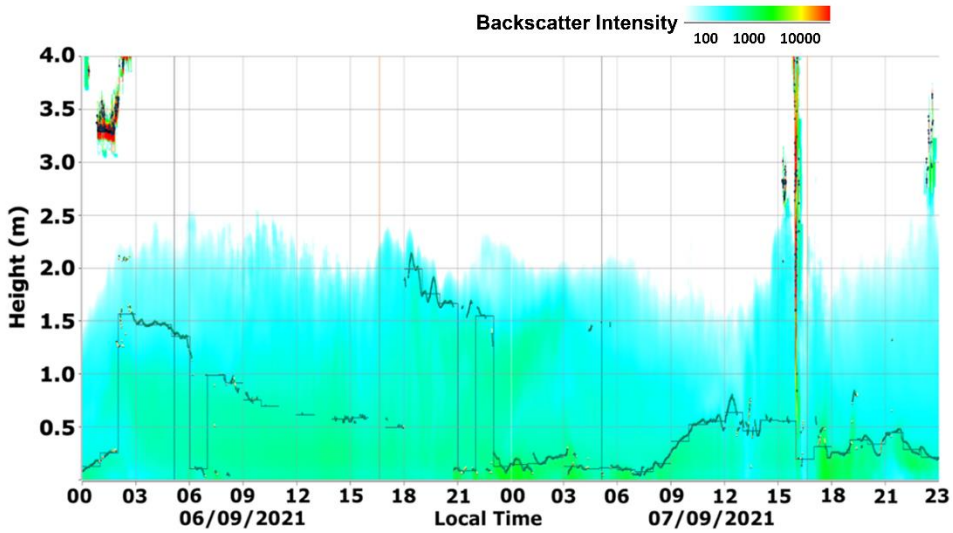

Figure 21: PBL structure as observed on 06 and 07 September 2021. The shallow PBL on September seventeenth resulted from the sinking motion of the atmosphere due to the presence of a high-pressure region over the study area.

3.4 Summary Graphs

It is of help to present a full picture after concluding our work in the characterization of BC and BrC optical parameters here in the El Paso – Ciudad Juarez airshed. Because of that, we have prepared five summarizing graphs, where each optical parameter is compared between the three seasons we studied.

From a quantitative point of view, Figure 22 compares the EBC Babs as measured by the PAX 870 nm at various seasons. The 3:00 PM-forward increment, in the winter data stands out from the other plots. Before that significant peak, we can appreciate the baseline behavior ranging mostly between 0 and 2 Babs (1/Mm). The spring tendency remains at the baseline, with smoother peaks slowly increasing and decreasing throughout a 24 hours period. The outline for the summer season (30 days plotted) combines the Babs measured during the wildfire events with those of baseline days, which reduced the overall average of the wave. Still, the shape of the curve is still visible as the trend rises from those of winter and spring.

The EBC Babs derivated from PAX 405 nm, is just what we observed with the PAX 870 nm times 2.148, which is the ratio between the two wavelengths. As such, the graph presents the

same tendencies and trend seen in the figure. It is significant to mention that the portion of the Babs measured by the PAX 405 nm which belong to EBC Babs, was often less than the 50% of the total Babs (as measured by the PAX 405): around 46.82% for the winter case, 34.7% for the spring case, 34.41% of the non-event days (baseline) of summer Babs, and 50.86% of the summer wildfire event days (eighteen days between August and September, 2021). The rest of the Babs measured by this instrument corresponded to that of brown carbon and mineral dust (still present however small).

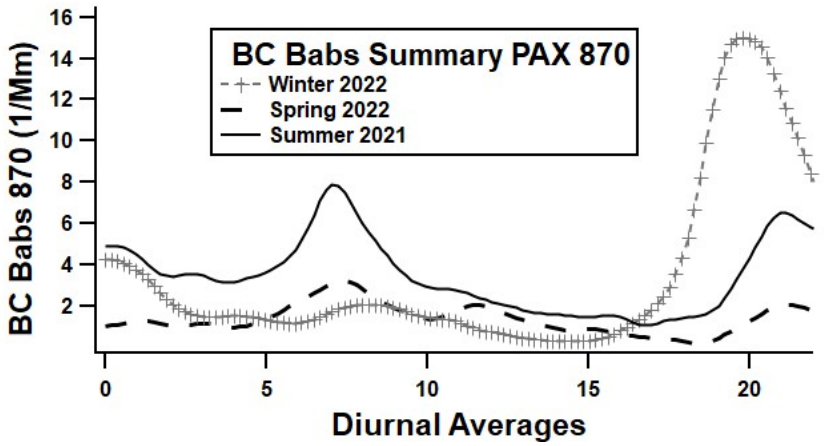

Figure 22: the Babs of the EBC particles as measured by the PAX 870 nm. The graph's legend indicates which plot trend belongs to each season characterization. The graph has a binomial smoothing filter applied.

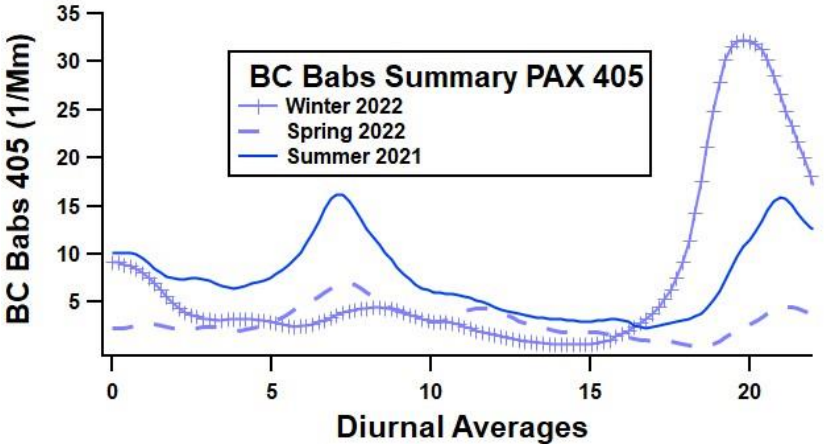

Figure 23: the Babs of the EBC particles as derived from the PAX 405 nm. Each trend line is 2.148 times bigger that those of the PAX 870. The graph's legend indicates which plot trend belongs to each season. The graph has a binomial smoothing filter applied

The BrC Babs comparison graph, Figure 24, shows, in general, a similar trend behavior than the performance of the waves that gave it birth. The peaks presence agrees with the rush hour times common in the international bridges. After subtracting the portion of the Babs measurements that belonged to EBC Babs (from PAX 405 nm), what is left is assumed to be BrC Babs (plus a negligible mineral dust Babs). The results exhibited a tendency that surprised us: the baseline Babs contained more BrC Babs than when a wildfire event happened: winter BrC portion was equal to 53.18%, spring BrC portion was equal to 65.30%, and the baseline Babs for summer contained 65.59% of BrC Babs. We can say that, as result of engine's incomplete internal combustion and the inefficient combustion of biomass burning from the brick kilns, the BrC particles yielded were more numerous than BC particles for this region. Quantitatively, the averaged BrC Babs values were greater during the wildfire events (EBC Babs were much higher as well) as one can see on Figure 24.

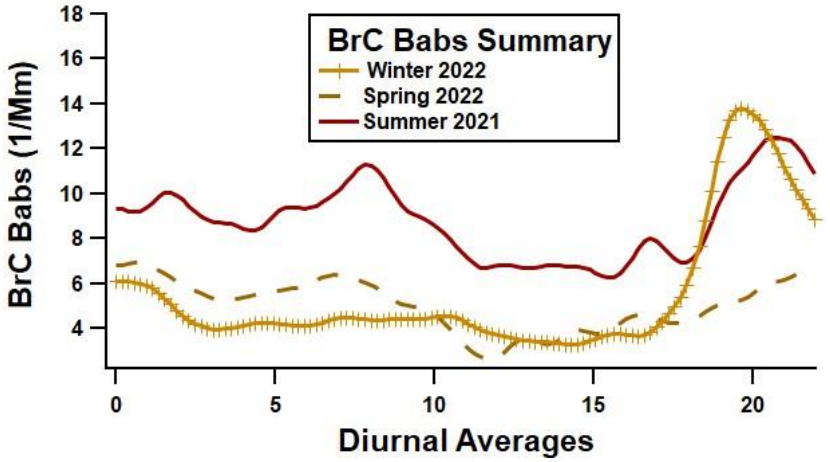

Figure 24: BrC Babs as calculated from equation (3). Though the plotting has a binomial smoothing filter, the trends seem noisy, maybe because the mineral dust particles contributed more to the total Babs than we expected. The peaks agree with the rush hour times customary for this region.

Figures 25 and 26 compares the optical parameter SSA and AAE for the three-seasons observed as measured by the PAX 870 nm. For Figure 25, the single scattering albedo is compared. Since this optical parameter refers to the scattering and absorption properties of the BC particles, we can clearly see that the winter season showed a lot more BC absorption than the others, and the

spring season was characterized by the presence of BC particles with heavy scattering properties. Summer rests right between the other two plots. Here, the summer SSA contains that of the baseline and wildfire event.

Figure 26 presents the behavior of the absorption Ångstrom exponent present in the three seasons. Winter and spring AAE follow a similar pattern with some paralleled peaks and valleys. Summer showed a more extreme performance in the sense that we see a greater spread of the data points. It is accepted by the literature that this optical parameter is related to a particle's size: inversely related to the size of particles. Summer displayed the greatest differences, which is to be expected as we had 18 days where BC-rich smoke clouds arrived to El Paso from the West coast wildfires.

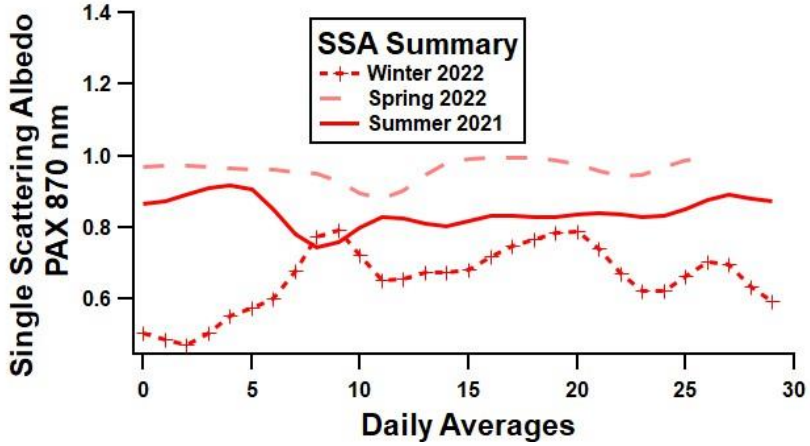

Figure 25: The SSA summary for the three seasons. Binomial smoothing filter applied

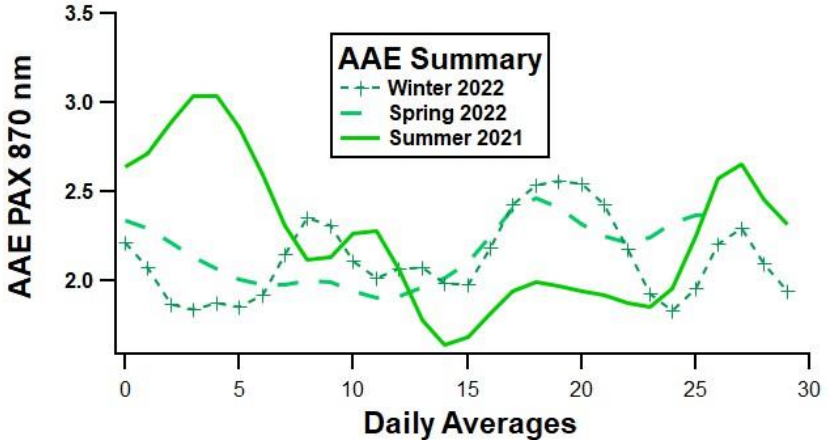

Figure 26: The AAE summary for the three seasons. Binomial smoothing filter applied.

Chapter 4: Discussion and Conclusions

The absorption coefficients were measured with two Photoacoustic Extinctiometers (PAX 405 nm and PAX 870 nm) to study the Babs due to black and brown carbon. The data we analyzed was denuded (at 340ºC) before entering the instruments. It is important to have that in mind for future studies that this work refers to denuded aerosols instead of ambient aerosols.

The winter and wildfire summer seasons in El Paso – Ciudad Juarez airsheds have specific season-related behavior that increased the amounts of Babs due to EBC and BrC from a baseline. This baseline was formed by the heavy international bridges vehicular traffic and by the brick kilns in Ciudad Juarez. The spring season displayed smoother tendencies driven by the local behavior that we called baseline. A well-established methodology to extract the brown carbon Babs from the PAX 870 and PAX 405 was used.

The winter season in this study (January 2022) showed that the Babs of black and brown carbon was caused by biomass burning in Ciudad Juarez, such as by the brick kilns, heavy traffic, and crossing time between cities. Black carbon is emitted from higher temperature combustion than brown carbon. The ratio of black carbon to brown carbon concentrations may be an indicator of the relative ratio of anthropogenic carbonaceous particulate emissions to wildfire emissions and this is a question for future research. The measured Babs formed a baseline. It was found that for the local time segment between 3:00PM and midnight, a considerable increment in the Babs of black and brown carbon was present. The increment was determined to be due to the burning of wood, charcoal, and other biomasses as an alternative space-heating system and open wood burning for meals' cooking during the colder winter season among the economically disadvantaged households in Ciudad Juarez. From the PAX 405 nm, Babs due to black carbon during this time segment increased by more than 180% from the baseline of the morning measurements. Finally, the brown carbon Babs for the discussed time segment increased a 154% from the baseline present in the morning measurements. When determining the percentages of the Babs due to black and brown carbon present in the atmosphere, we calculated that 53.74%

(±16.5%) of the total Babs (Babs) measured by PAX corresponded to the absorption of brown carbon particles. The TCEQ carbon monoxide graph behavior correlated well with our findings as a notorious rise of the averaged values for the late evening time segment was present in agreement with the literature. The single scattering albedo and the Absorption Ångstrom exponent for the season were also calculated. Both results were in accord with the presence of black and brown carbon particles in the atmosphere.

The spring season exhibited a smoother behavior of the EBC and BrC Babs. Though the peaks and valleys are still there, in agreement with rush hour times, the Babs values remained bounded between 0 and 5 (1/Mm). As commonly observed, the BrC Babs trend were noisier, which could be due to the nature of the BrC Babs calculation plus the presence of mineral dust Babs, that may not be as negligible as first expected. This remains to be studied in the future. The BrC Babs percentage, from the PAX 405 nm Babs, was higher than that of the two other seasons. This presents a surprise for us. Since we assumed that most of the baseline BC and BrC came from the idling traffic at the international bridges, it is interesting to notice that, if true, the pollution output by engine combustion has a high degree of BrC. It may be the case that the brick kilns are indeed the major contribution, and not the heavy traffic at the bridges. The AAE paralleled the behavior of the winter season. However, the SSA surprised us with the presence of mostly scattering particles.

The wildfire season characterization was facilitated by the extensive wildfire seasonal occurrences on the US West Coast. Given the right atmospheric conditions as stated in section 3.2.3, we concluded that smoke plumes from these wildfires were transported to our region on eighteen separate occasions (event days). This assertion was endorsed by the HRRR and HYSPLIT platforms. From the PAX 870 nm, mass concentration (µg/m3) due to EBC particles were obtained. It was determined that the West Coast wildfires added more than 58% of the total calculated mass concentration due to EBC in our airshed. Similarly, to the winter season defined in this paper, we also calculated a baseline for the summer season. The PAX 870 nm Babs showed values ranging between 0.6639 and 1.003 per megameter, with an average of 0.85 ± 0.50 (1/Mm).

In contrast, the PAX 405 nm Babs ranged between 3.7 and 7.7 per megameter, with an average of 5.9 ± 1.7 (1/Mm). This baseline had the same sources as the Winter's, mainly the particulate emissions of the commercial and vehicles waiting to cross between El Paso and Ciudad Juarez. From the eighteen wildfire event days, the Babs due to EBC measured with the PAX 870 nm averaged 2.9 ± 1.8 (1/Mm), signifying a 346% increment from its baseline, and the Babs derived from the PAX 405 nm averaged 11.43 ± 4.9 (1/Mm) with a 195% increment from its baseline. The BrC Babs average for event days was 5.2 ± 1.7 (1/Mm) and 3.8 ± 0.8 (1/Mm) for non-event days, implying a 137% increment. The single scattering albedo and the Ångstrom exponent for the selected wildfire season were also calculated. We observed that the Absorption Angstrom Exponent (AAE) for the summer wildfire season becomes smaller, in particular for particles with mean diameters larger than 0.12 micrometers, which is symptomatic that the BC particles that arrive in the El Paso region are aged.

We discussed the synoptic conditions associated with the EBC and BrC exceedances at the research site. The atmospheric conditions were predominantly stable due to prevalent synoptic conditions on those days. Growth of the PBL was restricted due to the stable conditions caused by the high-pressure system over the region. Lower PBL affected the vertical dispersion of the pollutants resulting into an increase in concentrations. The circulation patterns resulted due to high pressure systems in the north and low-pressure system in the south of the study area advected large smoke concentrations from the wildfire emission sources in the west of the US to the research site. The detailed analysis of September 6, 7 and 9 highlights the consequences of the synoptic-scale meteorological conditions and regional PBLHs, leading to detection of wildfire smoke in the El Paso-Juarez region.

Finally, the El Paso–Juárez metropolitan area is a diverse socio-economic area and is the United States' second-largest majority Hispanic city. The effect of seasonal, meteorological variations on particulate matter concentrations will aid in assessing the impact of climate change on desert regions, such as the El Paso-Juárez region with its diverse population.

Future work can be done on the local sources of Brown Carbon as we had assumed that BC would be the dominant of the two. Also it would be interesting to correlate more closely the wildfire season data with ozone, such VOC and NO_x. Creating scatter plots comparing effective BC with CO and NO_x would be beneficial in order to create a data set of these particles behavior in our region. Also, for the PAX 405 nm data, we assumed that mineral dust Babs was negligeable. It would be very interesting to find a way to verify that claim.

References

1. Polanco Gonzalez, J. An Improved Method for Optical Characterization of Mineral Dust and Soot Particles in the El Paso-Juárez Airshed Available online: http://148.210.21.170/handle/20.500.11961/16767 (accessed on November secondcond 2021).
2. Karle, N.N. Studies of the Planetary Boundary Layer and Their Impact on Air Pollution in a Semi-Arid Region with Complex Terrain. Ph.D. Dissertation, The University of Texas at El Paso: United States -- Texas, 2021.
3. Karle, N.N.; Mahmud, S.; Sakai, R.K.; Fitzgerald, R.M.; Morris, V.R.; Stockwell, W.R. Investigation of the Successive Ozone Episodes in the El Paso–Juarez Region in the Summer of 2017. *Atmosphere* **2020**, *11*, 532, doi:10.3390/atmos11050532.
4. Petzold, A., Ogren, J. A., Fiebig, M., Laj, P., Li, S.-M., Baltensperger, U., Holzer-Popp, T., Kinne, S., Pappalardo, G., Sugimoto, N., Wehrli, C., Wiedensohler, A., and Zhang, X.-Y.: Recommendations for reporting "black carbon" measurements, Atmos. Chem. Phys., 13, 8365–8379, https://doi.org/10.5194/acp-13-8365-2013, 2013.
5. Stuart K. Grange, Hanspeter Lötscher, Andrea Fischer, Lukas Emmenegger and Christoph Hueglin, Evaluation of equivalent black carbon source apportionment using observations from Switzerland between 2008 and 2018, Atmos. Meas. Tech., 13, 1867–1885, 2020. https://doi.org/10.5194/amt-13-1867-2020.
6. Esparza, A.E.; Fitzgerald, R.M.; Gill, T.E.; Polanco, J. Use of Light-Extinction Method and Inverse Modeling to Study Aerosols in the Paso Del Norte Airshed. *Atmos. Environ.* **2011**, *45*, 7360–7369, doi:10.1016/j.atmosenv.2011.07.039.
7. Fitzgerald, R.M.; Karle, N.N.; Lara, P.; Polanco Gonzalez, J.; Stockwell, W.R. Optical Measurements of Particulate Matter in the El Paso-Juarez Region: Natural Mineral Dust and Soot. *Environmental Manager,* **2021**.
8. Andreae, M.O.; Gelencsér, A. Black Carbon or Brown Carbon? The Nature of Light-Absorbing Carbonaceous Aerosols. *Atmospheric Chem. Phys.* **2006**, *6*, 3131–3148, doi:10.5194/acp-6-3131-2006.
9. Yan, J.; Wang, X.; Gong, P.; Wang, C.; Cong, Z. Review of Brown Carbon Aerosols: Recent Progress and Perspectives. *Sci. Total Environ.* **2018**, *634*, 1475–1485, doi:10.1016/j.scitotenv.2018.04.083.
10. Künzi, L.; Mertes, P.; Schneider, S.; Jeannet, N.; Menzi, C.; Dommen, J.; Baltensperger, U.; Prévôt, A.S.H.; Salathe, M.; Kalberer, M.; et al. Responses of Lung Cells to Realistic Exposure of Primary and Aged Carbonaceous Aerosols. *Atmos. Environ.* **2013**, *68*, 143–150, doi:10.1016/j.atmosenv.2012.11.055.
11. Stewart, D.R., E. Saunders, R.A. Perea, R. Fitzgerald, D.E. Campbell and W.R. Stockwell, Linking Air Quality and Human Health Effects Models: An Application to the Los Angeles Air Basin, Environmental Health Insights, 11, 1–13, 2017. doi: 10.1177/1178630217737551
12. Hand, JL; Kreidenweis, S.M.; Eli Sherman, D.; Collett, J.L.; Hering, S.V.; Day, DE; Malm, W.C. Aerosol Size Distributions and Visibility Estimates during the Big Bend Regional Aerosol and Visibility Observational (BRAVO) Study. *Atmos. Environ.* **2002**, *36*, 5043–5055, doi:10.1016/S1352-2310(02)00568-X.
13. Yang, M.; Howell, S.G.; Zhuang, J.; Huebert, B.J. Attribution of Aerosol Light Absorption to Black Carbon, Brown Carbon, and Dust in China – Interpretations of Atmospheric Measurements during EAST-AIRE. *Atmospheric Chem. Phys.* **2009**, *9*, 2035–2050, doi:10.5194/acp-9-2035-2009.

14. Kamm, S.; Möhler, O.; Naumann, K.-H.; Saathoff, H.; Schurath, U. The Heterogeneous Reaction of Ozone with Soot Aerosol. *Atmos. Environ.* **1999**, *33*, 4651–4661, doi:10.1016/S1352-2310(99)00235-6.
15. Ammann, M.; Kalberer, M.; Jost, D.T.; Tobler, L.; Rössler, E.; Piguet, D.; Gäggeler, H.W.; Baltensperger, U. Heterogeneous Production of Nitrous Acid on Soot in Polluted Air Masses. *Nature* **1998**, *395*, 157–160, doi:10.1038/25965.
16. Vedal, S.; Dutton, S.J. Wildfire Air Pollution and Daily Mortality in a Large Urban Area. Environmental Research 2006, 102, 29–35, doi:10.1016/j.envres.2006.03.008.
17. Chalbot, M.-C.; Kavouras, I.G.; Dubois, D.W. Assessment of the Contribution of Wildfires to Ozone Concentrations in the Central US-Mexico Border Region. Aerosol Air Qual. Res. 2013, 13, 838–848, doi:10.4209/aaqr.2012.08.0232.
18. June, N.A.; Hodshire, A.L.; Wiggins, E.B.; Winstead, E.L.; Robinson, C.E.; Thornhill, K.L.; Sanchez, K.J.; Moore, R.H.; Pagonis, D.; Guo, H.; et al. Aerosol Size Distribution Changes in FIREX-AQ Biomass Burning Plumes: The Impact of Plume Concentration on Coagulation and OA Condensation/Evaporation. Atmospheric Chemistry and Physics Discussions 2022, 1–35, doi:10.5194/acp-2022-349.
19. Liu, C.; Chung, C.E.; Yin, Y.; Schnaiter, M. The Absorption Ångström Exponent of Black Carbon: From Numerical Aspects. Atmospheric Chemistry and Physics 2018, 18, 6259–6273, doi:10.5194/acp-18-6259-2018.
20. Chen, Claudia. Characterization of Temperature Profiles in a Thermodenuder, UC Davis Undergraduate Research Journal, 15(2013)
21. Bond, T.C.; Bergstrom, R.W. Light Absorption by Carbonaceous Particles: An Investigative Review. *Aerosol Sci. Technol.* **2006**, *40*, 27–67, doi:10.1080/02786820500421521.
22. Karle, N.; Mahmud, S.; Fitzgerald, R.; Estes, M.; Walter, P.; Morris, G. Analysis of Boundary Layer Heights Using Ceilometer and Models in the El Paso-Juarez Airshed; 101st American Meteorological Society Annual Meeting, **2021**.
23. Washenfelder, R. A., Flores, J. M., Brock, C. A., Brown, S. S., and Rudich, Y.: Broadband measurements of aerosol extinction in the ultraviolet spectral region, Atmos. Meas. Tech., 6, 861–877, https://doi.org/10.5194/amt-6-861-2013, **2013**.
24. Kelly, K.; Wagner, D.; Lighty, J.; Núñez, M.Q.; Vazquez, F.A.; Collins, K.; Barud-Zubillaga, A. Black Carbon and Polycyclic Aromatic Hydrocarbon Emissions from Vehicles in the United States–Mexico Border Region: Pilot Study. *J. Air Waste Manag. Assoc.* **2006**, *56*, 285–293, doi:10.1080/10473289.2006.10464465.
25. Shi, Y.; Murr, L.E.; Soto, K.F.; Lee, W.-Y.; Guerrero, P.A.; Ramirez, D.A. Characterization and Comparison of Speciated Atmospheric Carbonaceous Particulates and Their Polycyclic Aromatic Hydrocarbon Contents in the Context of the Paso Del Norte Airshed Along the U.s.-Mexico Border. *Polycycl. Aromat. Compd.* **2007**, *27*, 361–400, doi:10.1080/10406630701624333.
26. Raysoni, A. Assessment of Intra-Urban Traffic-Related Air Pollution on Asthmatic Children's Exposure at Schools in the Paso Del Norte Region. *Open Access Theses Diss.* **2011**.
27. Alba Yadira Corral Avitia and Antonio De la Mora Covarrubias, Environmental Assessment of Brick Kilns in Chihuahua State, México, Using Digital Cartography, IntechOpen.com, 2012, 14, 261-281.
28. Montoya, T.; Guarian, P.L.; Velazquez-Angulo, G.; Corella-Barud, V.; Rojo, A., Graham, J.P. Carbon Monoxide Exposure in Households in Ciudad Juarez, Mexico. Int. J. Hyg. Environ. 2008, Health 211 40–49. Doi: 10.1016/j.ijheh.2006.12.001
29. Kirchstetter, T. W., Novakov, T., and Hobbs, P. V.: Evidence That the Spectral Dependence of Light Absorption by Aerosols is Affected by Organic Carbon, J. Geophys. Res., 109, D21208, 2004.

30. Lack, D.A.; Langridge, J.M. On the Attribution of Black and Brown Carbon Light Absorption Using the Ångström Exponent. *Atmospheric Chem. Phys.* **2013**, *13*, 10535–10543, doi:10.5194/acp-13-10535-2013.
31. Zhang, G., Peng, L., Lian, X., Lin, Q., Xinhui Bi, Duohong Chen, Mei Li, Lei Li, Xinming Wang, Guoying Sheng. An Improved Absorption Angstrom Exponent (AAE)-Based Method for Evaluating the Contribution of Light Absorption from Brown Carbon with High-Time Resolution. Aerosol and Air Quality Research, **2019**, 19: 15-24.
32. Yuan Liu, Guangzhi He, Biwu Chu, Qingxin Ma, Hong He, Atmospheric heterogeneous reactions on soot: A review Fundamental Research. preprint, 2022.
33. Stein, A.F.; Draxler, R.R.; Rolph, G.D.; Stunder, B.J.B.; Cohen, M.D.; Ngan, F. NOAA's HYSPLIT Atmospheric Transport and Dispersion Modeling System. *Bull. Am. Meteorol. Soc.* **2015**, *96*, 2059–2077, doi:10.1175/BAMS-D-14-00110.1.
34. Baumgardner, D., G. Raga, O. Peralta, I. Rosas, T. Castro, T. Kuhlbusch, A. John, A. Petzold, 2002: Diagnosing Black Carbon Trends in Large Urban Areas Using Carbon Monoxide Measurements, *J. Geophys. Res.*, 10.1029/2001JD000626.
35. Takemura, T.; Nakajima, T.; Dubovik, O.; Holben, B.N.; Kinne, S. Single-Scattering Albedo and Radiative Forcing of Various Aerosol Species with a Global Three-Dimensional Model. Journal of Climate 2002, 15, 333–352, doi:10.1175/1520-0442(2002)015<0333:SSAARF>2.0.CO;2.
36. Schuster, G.; Dubovik, O.; Holben, B. N. Angstrom Exponent and Bimodal Aerosol Size Distribution; Journal of Geophysical Research, vol. 111, D07207, doi:10.1029/2005JD006328, 2006.
37. Karle, N.N.; Fitzgerald, R.M.; Sakai, R.K.; Sullivan, D.W.; Stockwell, W.R. Multi-Scale Atmospheric Emissions, Circulation and Meteorological Drivers of Ozone Episodes in El Paso- Juárez Airshed. Atmosphere 2021, 12, 1575, doi:10.3390/atmos12121575.
38. Einfeld, W.; Church, HW; Yarbrough, J.W. *Winter Season Air Pollution in El Paso-Ciudad Juarez*; US Environmental Protection Agency, Region VI, Air, Pesticides & Toxics Division, **1995**.
39. Liu, Y.; He, G.; Chu, B.; Ma, Q,; He, H; Atmospheric heterogeneous reactions on soot: A review Fundamental Research. preprint, 2022.http://www.keaipublishing.com/en/journals/fundamental-research/
40. June, N.A.; Hodshire, A.L.; Wiggins, E.B.; Winstead, E.L.; Robinson, C.E.; Thornhill, K.L.; Sanchez, K.J.; Moore, R.H.; Pagonis, D.; Guo, H.; Campuzano-Jost, P.; Jimenez, J.L.; Coggon, M.M.; Dean-Day, J.M.; Bui, T.P.; Peischl, J.; Yokelson, R. J.; Alvarado, M.J.; Kreidenweis, S.M.; Jathar, S.H.; Pierce, J.R.: Aerosol size distribution changes in FIREX-AQ biomass burning plumes: the impact of plume concentration on coagulation and OA condensation/evaporation. Atmos. Chem. Phys. Discuss. [preprint], **2022,** in Review.https://doi.org/10.5194/acp-2022-349, in review,. https://acp.copernicus.org/preprints/acp-2022-349/
41. Wagner, F.; Silva, A. M. Some Consideration about Angstrom Exponent Distribution. Atmos. Chem. Phys. 8, 481 -489, **2008.** https://doi.org/10.5194/acp-8-481-2008
42. Cheng, T.; Wu, Y.; Gu, X.; Chen, H. Effects of Mixing States on the Multiple-Scattering Properties of Soot Aerosols. Optic Express. 23, 8, 10808 – 1082, **2015,** https://doi.org/10.1364/OE.23.010808.

Vita

Pamela Lara is a dedicated Atmospheric Science professional graduating with a Ph.D. in Environmental Science and Engineering from the University of Texas at El Paso. She also received an MS in Physics from the same university, and a BS in Physics, from Utah Valley University.

Ms. Lara migrated to the US, from Chile, after graduating from Universidad Central with a Law degree.

Contact information: pilara@miners.utep.edu, PamLara2022@gmail.com,
www.linkedin.com/in/pamlara2022